

Norwegian University of Science and Technology

MASTER'S THESIS

The Importance of Friction Reduction in Boundary Layers

Julian de Kat

July 2019

Department of Marine Technology

Supervisor: Sverre Steen

Co-supervisor: Luca Savio

Co-supervisor: Juan Francisco Fuentes Pérez

Abstract

The modification of boundary layers for the purpose of drag reduction and overall propulsive efficiency for marine vehicles is an interesting concept, one which has been studied through swimming fish, which can alter the boundary layer actively and passively. Through research and biomimetic design, drag reduction by modifying the boundary layer could have a large impact on saving save fuel consumption and decreasing emissions significantly for marine vehicles.

This project aimed to investigate the flow properties of a hydrofoil and the effect of anti-fouling coating on the development of the boundary layer. The study aimed to answer two questions: first whether it is possible to determine boundary layer separation with on-board differential pressure sensors; and second to observe how a change in skin friction influences the boundary layer and investigate whether anti-fouling coating can delay the point of separation.

To investigate the boundary layer, a foil prototype was designed and subsequently built at the Center for Biorobotics Laboratory at TalTech in Tallinn, Estonia. The prototype is a standard NACA0025 foil and has 10 built-in differential pressure sensors along the chord length of the foil to measure the flow on the surface of the foil. With the help of the prototype, this research was done by looking at pressure distributions over the surface of the hydrofoil, compared with the measured forces on the foil. The change of pressure over the various angles, Reynolds numbers and chord length was taken into account.

The foil was tested in a towing tank, where the foil was towed at three different Reynolds numbers: $Re_1 = 2.035 \cdot 10^5$, $Re_2 = 4.07 \cdot 10^5$ and $Re_3 = 6.105 \cdot 10^5$. Lift and drag forces as well as differential pressures were measured at various angles of attack, with special interest in the stalling region. All of test conditions of the ucoated foil were supposed to have been repeated for the coated foil, but could not be done because of leaking problems encountered. Only a few angles were measured.

An analysis of the measured forces and pressured showed the following: Separation can be observed at stalling angles with the differential pressure sensors. For the coated foil, maximum lift coefficient is higher than for the coated foil and the stalling region is delayed, stalling at $\alpha > 35^\circ$. Overall, lift coefficient is increased with the anti-fouling coating, while drag coefficient is also increased.

The results from this research project suggest that coating a foil with a hydrophobic anti-fouling paint could shift the occurrence of stalling towards higher angles of attack. The potential relevance for marine vehicles should be evaluated further.

Acknowledgements

First and foremost I would like to thank my supervisor Sverre Steen sincerely for all the guidance, helping me through difficult subject matter and challenging setbacks. I would like to thank Jon Coll Mossige who helped me through various problems, Daniel Grieb for his research and guidance, and the NTNU-Berkeley Peder Saether group for the research and opportunities. Sincere thanks to Sintef Ocean for being able to do tests in the towing tank, and special thanks to Terje Rosten, Robert Opland, Luca Savio and Sverre Steen for guiding me through the tests. Then, very special thanks for Maarja Kruusmaa for letting me be part of the fantastic Centre for Biorobotics laboratory at Tallinn University of Technology, Tallinn, Estonia. And to Juan Francisco Fuentes-Pérez who built the hydrofoil and helped me design it. My sincere gratitude to both of them for their guidance, time, resources and this opportunity. I would like to extend my gratitude to others in the laboratory who helped me with the design and who helped me getting settled in Tallinn, specifically Asko Ristolainen and Mihkel Läänelaid. Working among the people in the Centre for Biorobotics and discovering Estonia was an amazing experience. Thanks to Angelika Brink and Tommy Ness Thorstensen of the Jotun company for taking special care of the foil and painting it with the anti-fouling paint.

Contents

Abstract	i
Acknowledgements	ii
List of Figures	vi
1 Introduction	1
2 Problem Definition	3
3 Theoretical Background	4
3.1 Laminar Boundary Layers	4
3.1.1 Governing Equations	5
3.1.2 Prandtl's Boundary Layer Equations	5
3.1.3 Blasius' Solutions	6
3.1.4 Von Karman Momentum Analysis	8
3.1.5 Total Drag Force	9
3.2 Turbulent Boundary Layers: Flow Separation	9
3.2.1 Vortex Shedding	10
3.3 Foil Dynamics	11
3.4 Pressure Distribution	12
3.4.1 Thickness Characteristics and 3D Effects	12
3.4.2 Pressure Gradients in Boundary Layer	15
3.5 Examples in Practice	16
3.5.1 Air Lubrication of Ship Hulls	16
3.5.2 Superhydrophobic Surfaces	17
3.5.3 Friction Reduction in Boundary Layers	18

4	Foil Prototype Design	19
4.1	Detailed Design	19
5	Experimental Setup	24
5.1	Test Setup	24
5.2	Test Conditions	26
5.2.1	Test Runs	26
5.2.2	Anti-Fouling Coating	28
5.3	Leaking Problems	29
6	Results	31
6.1	Force Analysis Uncoated	31
6.2	Force Analysis Coated	32
6.3	Differential Pressure Distributions	33
6.3.1	Uncoated	34
6.3.2	Comparison of Coated and Uncoated Data	41
6.3.3	Precision of the Pressure Sensors	43
6.4	Frequency Analysis	44
7	Discussion	48
8	Conclusions and Recommendations	49
8.1	Conclusions	49
8.2	Recommendations for Further Work	49
9	References	51
A	MPXV7002 Differential Pressure Sensor	53
B	iRon II Dataset	66

List of Figures

1	Water droplets resting on a lotus leaf	1
2	Development of boundary layer on a surface. [1]	4
3	Blasius' velocity distribution in the boundary layer [2]	7
4	Boundary layer development to flow separation	9
5	Development of vortex street with increasing Reynolds number [3].	10
6	Forces on cylinder in steady flow. [4]	11
7	Skin friction due to laminar boundary layer [1].	12
8	NACA0025 Profile	13
9	Boundary layer separation for two foils at $Re_2 = 4.070 \cdot 10^5$ and $\alpha = 15^\circ$. Derived from XFOIL [5].	14
10	C_L as a function of α for NACA0025 for three Reynold's numbers. Derived from XFOIL.	14
11	Influence of pressure gradient on velocity profile in the boundary layer [2]	16
12	Three methods for air lubrication: (a) Bubble Drag Reduction, (b) Air Layer Drag Reduction, (c) Partial Cavity Drag Reduction. [6]	17
13	Contact angle for SHS	17
14	Slip condition for friction reduction surfaces	18
15	Design of the iRon foil prototype [7]	19
16	Side view without clamp. Dimensions in m	20
17	Top view with clamp. Dimensions in mm	20
18	Distance between the pressure holes on the chord line in mm	21
19	Layout of the holes. Courtesy of Juan Francisco Fuentes-Pérez (Appendix B)	21
20	Section half of the foil with s9 and the foil's tubing structure. Holes 5, 7 and 9 are shown.	22
21	Finished prototype. Courtesy of Juan Francisco Fuentes-Pérez.	23
22	Foil set up in the rig	24

23	Sketch of the test setup in the water.	25
24	Definition of positive angle of attack.	25
25	Gap between surface-piercing foil and the prototype.	26
26	a) cylinder fastened to foil clamp. b) angle indicator. c) clamp holding cylinder in place. d) ensures cylinder does not fall when clamp c is loosened. e) angle wheel. f) force gauges.	27
27	Angle wheel indicating the angle of attack	27
28	Coated foil with rough edges around the sensors' measuring points.	29
29	Waterlogged foil.	30
30	Mean C_L and C_D as a function of α	31
31	a) Force coefficients for Re_3 and b) C_L/α as a function of α for three Reynolds numbers.	32
32	Mean C_L and C_D as a function of α for two Reynolds numbers for the coated foil.	32
33	a) Force coefficients for Re_3 and b) C_L/α as a function of α for three Reynolds numbers for coated foil.	33
34	Run 1201 with the signals of three pressure sensors on the suction side.	34
35	Mean differential pressure distribution and standard deviation over chord length for $\alpha = 15^\circ$ and $\alpha = 20^\circ$	35
36	Mean differential pressure distribution and standard deviation over chord length for $\alpha = 25^\circ$ and $\alpha = 28^\circ$	36
37	Mean differential pressure distribution and standard deviation over chord length for $\alpha = 30^\circ$ and $\alpha = 32^\circ$	36
38	Mean differential pressure distribution and standard deviation over chord length for $\alpha = 33^\circ$ and $\alpha = 35^\circ$	37
39	Mean differential pressure distribution and standard deviation over chord length for $\alpha = -20^\circ$ and $\alpha = -32^\circ$	37
40	Standard deviation of C_p averaged over all runs as a function of α for all sensors for three Reynolds numbers.	38
41	Time series of dp signals for run 322.	39
42	Time series of force signals for run 322 during u_1	40
43	Time series of dp signals for run 352.	40

44	Time series of force signals for run 352.	41
45	Comparison of differential pressure distribution over chord length for $\alpha = 28^\circ$ and $\alpha = 30^\circ$ for uncoated and coated foil.	41
46	Comparison of differential pressure distribution over chord length for $\alpha = 32^\circ$ and $\alpha = 33^\circ$ for uncoated and coated foil.	42
47	Comparison of differential pressure dist for $\alpha = 35^\circ$ standard deviations of sensors as a function of α for coated foil.	42
48	Two examples of repeated runs and their mean.	43
49	Standard deviation of all runs combined as a function of alpha for sensor 2. . . .	43
50	Standard deviation of all runs combined as a function of alpha for four sensors. .	44
51	Strouhal number as a function of alpha at $Re = 5 \cdot 10^5$ for three profiles: (a) NACA0015, (b) NACA0025 and (c) NACA0035. [8]	45
52	Spectral density of lift as a function of frequency for various 25 and 30 degrees. .	46
53	Spectral density of lift and drag as a function of frequency for 33 degrees. . . .	46
54	Spectral density of lift force signal as a function of frequency for $\alpha = 35^\circ$	47
55	Spectral density of sensor signals as a function of frequency for $\alpha = 35^\circ$	47

1 Introduction

In the study of hydrodynamic boundary layers, special attention has been given over the years to swimming fish and other aquatic animals, because of their efficient locomotive propulsion and ability to reduce drag. In fact, there are two ways in which fish can control the flow around their bodies: both passively, due to shape and form, and actively, through sensory organs (lateral lines) directing muscular control to change the flow directly [9]. By controlling the flow, fish prevent flow separation, effectively reducing drag [10]. It is the flow sensory capabilities of fish' lateral lines that inspired artificial lateral line probe [11] for calculating velocities of AUVs at the Centre for Biorobotics at Tallinn University of Technology. Here, differential pressure sensors are used to measure local pressures along the body to actively control AUVs.

The modification of boundary layers for the purpose of drag reduction and overall propulsive efficiency is indeed very interesting, which could have a large impact on marine vehicles, as reducing skin-friction drag could save fuel consumption and emissions significantly. Skin-friction drag reduction methods have been studied in the past, for example air bubble lubrication for ship hulls. Another example, which also incorporates boundary layer alteration, comes from the inspiration of the lotus leaf and its super-hydrophobic properties. Figure 1 shows the result of this principle, in which water droplets have been shaped into almost perfect spheres resting on the lotus leaf's surface. Studies have been done to investigate the drag reduction capabilities of super-hydrophobic surfaces in relation to turbulent flow, which has been proven promising [12]. There is more to learn from super-hydrophobic materials to gain knowledge of their full potential.



Figure 1: Water droplets resting on a lotus leaf

This project aims to investigate the flow properties of a hydrofoil and originally, what effect a super-hydrophobic coating has on the boundary layer. A suitable hydrophobic coating could not be found, and instead the effect of an anti-fouling paint is analyzed. The flow is analyzed with the aforementioned differential pressure sensors, to observe changes in the boundary layer and to see if there is delay in separation.

A reason to investigate whether it is possible to determine boundary layer separation, or changes in boundary layer with on-board differential pressure sensors, is that they could potentially be

used as active controls in the future and could be applicable to a wide range of marine vehicles.

First, it could give insight to stalling regions of lifting surfaces such as foils or rudders, which could be helpful for stabilizing hydrofoil vessels. It could also be used to stabilize UAVs at higher speeds, where the pressure sensors could give feedback to flaps and propulsion systems. If the differential pressure sensors could give an indication of when a vehicle is about to stall, and if this information could be used to actively control the vehicle to prevent stall, it would be a significant step forwards in marine craft innovation.

Limitations

The tests are to be done in high Reynolds number flow, which gives limitations to the span of the foil, as the force transducers have an upper limit. With a large span, the lift force could easily become too large for the force transducer. Another limiting factor is the 3D printer dimensions which limit the size of the prototype.

Another limitation is the absence of hydrophobic paint, which was originally planned to be investigated. A quick solution was to paint the foil with hydrophobic paint. The drawback is the lack of knowledge of the paint characteristics, such as the thickness, brittleness and the skin friction characteristics.

A major setback was that the foil leaked during the coated tests, which limits the comparison between coated and uncoated foil. Data processing was very time consuming which limited the amount able to be processed.

2 Problem Definition

This thesis aims to investigate the boundary layer flow around a hydrofoil and consists of two main parts:

1. To investigate whether it is possible to determine boundary layer separation with on-board differential pressure sensors.
2. Observe how anti-fouling coating influences the boundary layer and investigate whether it can delay the point of separation.

The above points are investigated as follows. A NACA0025 hydrofoil equipped with differential pressure sensors is placed under water at various angles of attacks for various Reynolds numbers. Forces in x and y -directions are measured to determine the stall region of the foil. Pressure along both surfaces of the foil is measured by the built-in sensors. The hydrofoil is then coated with a hydrophobic paint and the measurements are repeated.

Detailed Approach

The aim of Part 1 is to assess what can be determined through the built-in pressure sensors to find full potential of the sensors, and to see if they could perhaps be used as active controls in practice for future hydrofoils of marine vehicles. The following questions are aimed to be answered in terms of the pressure measurements in combination with the measured x and y -forces:

- Can the separation point of the boundary layer be estimated/determined?
- How does the differential pressure develop over chord length?
- Is it possible to detect (alternating) vortex shedding?

The above will be answered by looking at pressure distributions over the surface of the hydrofoil and the pressure fluctuations, comparing this with the measured forces on the foil. The change of pressure over the angle of attack, Reynolds numbers and chord length will be taken into account.

Part 2 aims to investigate how skin friction reduction influences the boundary layer. We aim to analyze how anti-fouling coating influences boundary layer development and flow separation of a foil in a constant freestream velocity. Then it will be compared to the uncoated foil. This will be done by answering the following questions:

- Will there be differences in lift force compared to the uncoated case?
- What are the differences in drag force for zero angle of attack for the two cases?
- How does the differential pressure profile change?

3 Theoretical Background

The purpose of this section is to give an overview of viscous flow theory and flow separation and to give an overview of what methods are used to reduce skin friction on bodies in water (e.g. air lubrication techniques and super-hydrophobic surfaces). The goal is to investigate how skin friction impacts the boundary layer and flow separation. The investigation will be focused on a foil in water.

The following will be answered:

- Under what conditions does flow separation occur?
- To what extent is this important for marine vehicles?
- How can the separation point of a foil be determined experimentally?

To understand how friction reduction techniques may influence the boundary layer, a good understanding of the boundary layer is needed. This section gives an outline of the effect of viscosity on fluid flow and gives solutions to the governing equations of boundary layers. We will go through laminar and turbulent boundary layers and how they influence the viscous drag.

3.1 Laminar Boundary Layers

Let us consider an infinite and viscous fluid in a steady flow U_0 and a solid body in this infinite fluid. If the flow is not too fast and the body is somewhat streamlined, no separation occurs and because of viscous effects a thin laminar boundary layer is created above the surface of the body. The body has a no-slip condition at its surface where the fluid has zero velocity. The boundary layer of the fluid is the layer near the surface where the velocity speeds up from zero velocity to its steady flow velocity U_0 , as shown in Figure 2. Here, the steady flow velocity is indicated as U_∞ .

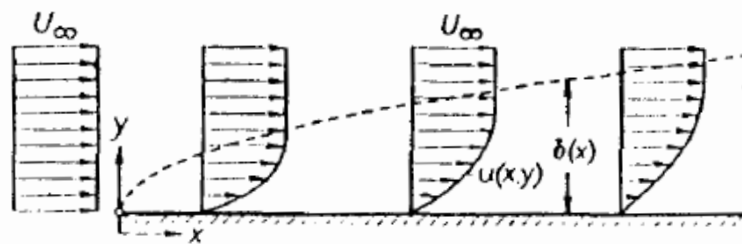


Figure 2: Development of boundary layer on a surface. [1]

The difference in flow velocity through the boundary layer and the whole reason why there is

a boundary layer is due to the shear stress between the viscous fluid and the wall of the body. Later we will see that it is this that causes the skin friction resistance on the body.

3.1.1 Governing Equations

A non-dimensional parameter called the Reynold's number Re is used to relate the viscous terms to the speed of the fluid:

$$Re = \frac{U_0 L}{\nu} \quad (1)$$

Where L is the characteristic length of the object and ν is the kinematic viscosity, $\nu = \mu/\rho$. Considering the characteristic length, if the object is a flat plate, for example, and one wants to calculate the Reynold's number at a certain point of the plate, the characteristic length is then substituted by x , the point at which the Reynold's number is to be used. This is indicated with a subscript, Re_x and defined as:

$$Re_x = \frac{U_0 x}{\nu} \quad (2)$$

Governing equations and characteristics of the boundary layer [1]:

Continuity:

$$\frac{\partial u}{\partial x} + \frac{\partial v}{\partial y} = 0 \quad (3)$$

Two-dimensional Navier-Stokes equations (in x and y):

$$u \frac{\partial u}{\partial x} + v \frac{\partial u}{\partial y} = -\frac{1}{\rho} \frac{\partial p}{\partial x} + \nu \left(\frac{\partial^2 u}{\partial x^2} + \frac{\partial^2 u}{\partial y^2} \right) \quad (4)$$

$$u \frac{\partial v}{\partial x} + v \frac{\partial v}{\partial y} = -\frac{1}{\rho} \frac{\partial p}{\partial y} + \nu \left(\frac{\partial^2 v}{\partial x^2} + \frac{\partial^2 v}{\partial y^2} \right) \quad (5)$$

with the boundary conditions:

$$\begin{aligned} \text{at } y = 0 : \quad & u = 0 \text{ and } v = 0 \\ \text{at } y = \infty : \quad & u = U(x) \end{aligned}$$

3.1.2 Prandtl's Boundary Layer Equations

With approximations and simplification of the previous equations, Prandtl made an estimation for the boundary layer thickness δ . By substituting the previous boundary conditions and assuming $\partial p/\partial y = 0$, the Navier-Stokes equations simplify to

$$u \frac{\partial u}{\partial x} + v \frac{\partial u}{\partial y} = -\frac{1}{\rho} \frac{\partial p}{\partial x} + \nu \frac{\partial^2 u}{\partial y^2} \quad (6)$$

In general, the boundary layer thickness is proportional to the square root of the kinematic viscosity: $\delta \sim \sqrt{\nu}$ [1]. Prandtl's estimation of the boundary layer thickness is given by:

$$\frac{\delta}{L} \sim \frac{1}{\sqrt{Re}} = \sqrt{\frac{\nu}{UL}} \quad (7)$$

For a flat plate:

$$\frac{\delta}{x} \approx \frac{5.5}{\sqrt{Re_x}} \quad (8)$$

The main assumption of the boundary layer is that the shear layer is very small compared to the length of the object: $\delta \ll x$ [3]. For this to be true, the Reynold's number Re_x has to be much larger than 1 and the following can be stated:

For $Re_x \gg 1$:

$$\begin{aligned} \delta &\ll x \\ v &\ll u \\ \frac{\partial u}{\partial x} &\ll \frac{\partial u}{\partial y} \\ \frac{\partial v}{\partial x} &\ll \frac{\partial v}{\partial y} \end{aligned}$$

3.1.3 Blasius' Solutions

By introducing the variable

$$\eta = \frac{y}{x} \sqrt{Re_x} \quad (9)$$

and the nondimensional stream function

$$\psi_1 = \int_0^\eta \frac{u}{U_0} d\eta = f(\eta) \quad (10)$$

Blasius simplified Equation 6 to find a solution for the boundary layer equation for zero pressure gradient ($\partial p/\partial x = 0$), i.e. a flat plate [2]. Substituting

$$u = \frac{\partial \psi}{\partial y} = \frac{\partial \psi}{\partial \eta} \frac{\partial \eta}{\partial y} \quad (11)$$

and

$$v = -\frac{\partial \psi}{\partial x} = -\frac{\partial \psi}{\partial \eta} \frac{\partial \eta}{\partial x} \quad (12)$$

into Equation 6, the solution is of the form

$$f'(\eta)f''(\eta) + 2f'''(\eta) = 0 \quad (13)$$

with the following boundary conditions:

$$\begin{aligned} f(\eta) &= 0 \text{ for } \eta = 0 \\ f'(\eta) &= 1 \text{ for } \eta \rightarrow \infty \\ f''(\eta) &\rightarrow 0 \text{ for } \eta \rightarrow \infty \end{aligned}$$

The solution for Equation 13 was calculated by Taylor series expansion and the results are shown in Figure 3.

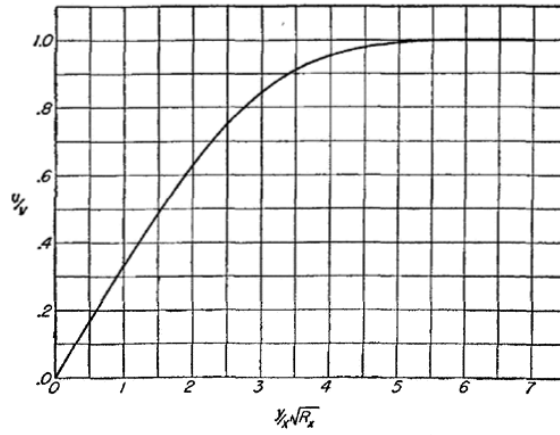


Figure 3: Blasius' velocity distribution in the boundary layer [2]

Two other values can be obtained through Blasius' solutions. One is the friction coefficient of a flat plate [2]

$$C_F = \frac{1.328}{\sqrt{Re_x}} \quad (14)$$

and what is called the displacement thickness, which is defined as the thickness where the flow velocity is 99% of the incident flow velocity $0.99U_0$. It is defined by

$$\delta^* = \frac{1}{U} \int_0^\delta (U - u) dy \quad (15)$$

Where U is the velocity right outside the boundary layer [2]. For a flat plate:

$$\frac{\delta^*}{x} = \frac{1.73}{\sqrt{Re_x}} \quad (16)$$

3.1.4 Von Karman Momentum Analysis

By making a momentum analysis in x and y for a flat plate some other useful variables can be obtained, as well as give a different approach to known ones. We assume that the edge of the plate is at $(x, y) = (0, 0)$. The flow past the plate will cause a frictional drag force D and due to the no-slip condition, it will obtain a velocity profile $u(y)$ dependent on the vertical coordinate at a horizontal location x . We assume that the pressure remains constant through the boundary layer, so $\partial p / \partial y = 0$. From this we can obtain the displacement thickness [3]:

$$\delta^* = \int_{y=0}^{y=h} \left(1 - \frac{u}{U}\right) dy \quad (17)$$

as h goes to infinity. The displacement thickness can also be defined as the distance a solid surface would have to be displaced to maintain the same mass flow rate as for non-viscous flow [3]. Conservation of momentum in x results also in the momentum thickness θ :

$$D = \rho \int_0^{h=\delta} u(U - u) dy \quad (18)$$

$$\theta = \frac{D}{\rho U^2} = \int_0^\delta \frac{u}{U} \left(1 - \frac{u}{U}\right) dy \quad (19)$$

And substituting θ and δ^* into the Von Karman Integral relation [2]

$$-\frac{dU}{dx} \int_0^\delta u(U - u) dy - \frac{d}{dx} \int_0^\delta u(U - u) dy = -\frac{\tau}{\rho} \quad (20)$$

we get

$$\frac{d\theta}{dx} + (H + 2) \frac{\theta}{U} \frac{dU}{dx} = \frac{\tau}{\rho U^2} \quad (21)$$

Where H is the shape parameter

$$H = \frac{\delta^*}{\theta} \quad (22)$$

3.1.5 Total Drag Force

The shear stress at the wall ($y = 0$) is defined by:

$$\tau = \mu \left. \frac{du}{dy} \right|_{y=0} \quad (23)$$

The viscous drag, or skin friction, associated with a laminar boundary layer is found by integrating the shear stress at the wall over the surface of the body:

$$D = b \int_{s=0}^L \tau_0 \cos \phi \, ds = b\mu \int_{x=0}^L \left. \frac{du}{dy} \right|_{y=0} dx \quad (24)$$

It is the velocity gradient at the wall, $\int_{x=0}^L \left. \frac{du}{dy} \right|_{y=0}$, that determines the drag. We will see in the following section that in a turbulent boundary layer, the velocity gradient is steeper.

3.2 Turbulent Boundary Layers: Flow Separation

The transition from laminar to turbulent flow results in a development of the boundary layer caused by an adverse pressure gradient in the boundary layer. This transition occurs when the pressure gradient on a surface counteracts the shear stress of a surface due to viscosity. A negative pressure gradient ($dp/dx < 0$) is called favorable, whereas a positive pressure gradient is unfavorable and often called the adverse pressure gradient.

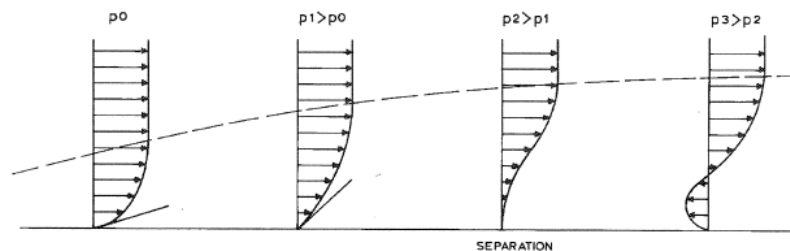


Figure 4: Boundary layer development to flow separation

As the fluid continues to flow towards an increasing pressure gradient, the wall shear stress becomes steeper and the velocity profile changes as shown in Figure 4. When the velocity gradient becomes too high compared to the wall shear stress, the flow separates and flows in the negative x -direction, causing eddies and momentum exchange in the boundary layer. The boundary layer becomes much thicker and the wake becomes larger.

3.2.1 Vortex Shedding

With local flow moving in the opposite direction of the initial flow, a vortex can form. With enough energy, the vortex will shed and boundary layer separation occurs. We will look at the case of a circular cylinder in a steady flow, where the Reynolds number for a cylinder is defined by its diameter D :

$$Re = \frac{UD}{\nu} \quad (25)$$

With low Reynold's number, eddies can form behind the cylinder but do not yet shed. With higher Reynold's numbers, as shown in Figure 5, vortices from each side of the cylinder will shed alternately with a shedding frequency f_v . Figure 5 only goes up to $Re = 281$ but alternating vortices are still present at $Re = 10^7$, even though the wake is turbulent and chaotic [3].

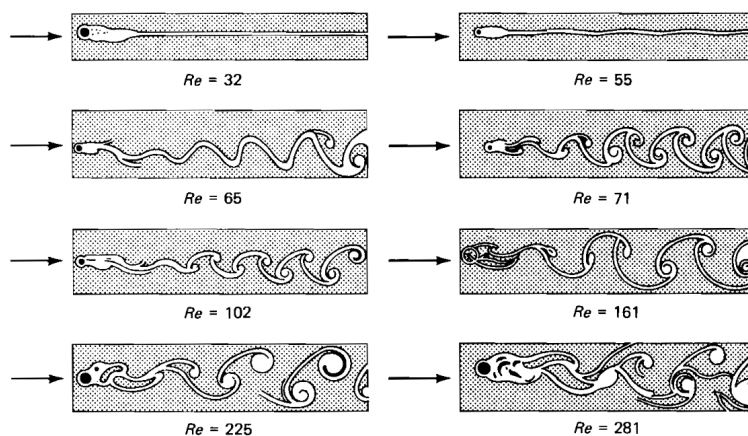


Figure 5: Development of vortex street with increasing Reynolds number [3].

The Strouhal number (Equation 26) is the non-dimensional form of the vortex shedding frequency and relates this variable to the incoming flow U and diameter D .

$$St = \frac{f_v D}{U} \quad (26)$$

Shedded vortices form a vortex street, called a Von Kármán vortex street, in the wake of the

cylinder as shown in Figure 5. The alternating shedding vortices influence the lift and drag forces on the cylinder as defined in Figure 6. The lift force will alternate from positive y to negative y , oscillating with the vortex shedding frequency f_v . The drag force changes only in magnitude and oscillates with $2f_v$. Note that lift force is always perpendicular to the incoming flow, thus always perpendicular to the drag force, and that drag force is always parallel with the flow.

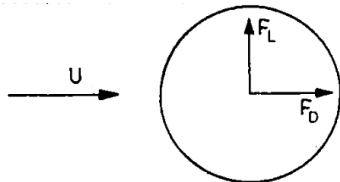


Figure 6: Forces on cylinder in steady flow. [4]

3.3 Foil Dynamics

Consider a foil deeply submerged in a viscous fluid so that there are no surface effects, the total drag can be decomposed into two main drag components: skin friction drag associated with viscous effects and pressure drag, associated mainly with the shape (form) of the foil. The pressure drag consists mainly of the form drag and induced drag and is large when an object in a fluid is not streamlined. For example, for a flat plate in perpendicular flow, the total drag consists of only pressure drag due to its form. A circular cylinder also has a large form drag and the skin friction drag can account for as low as 5% of the total drag for small Reynold's numbers [13]. For a streamlined body such as a foil (at small α) the pressure drag is less significant, the skin friction drag can account for between 40% and 80% of the total drag [13]. It is therefore useful to minimize the skin friction drag.

Let us now consider an uncambered foil with a (very) small angle of attack $\alpha < 5^\circ$ and a large Reynold's number $Re \approx 6 \cdot 10^6$. In these circumstances, the flow creates a thin laminar boundary layer near the surface of the foil and a small wake downstream. [3]. The 2D lift coefficient of the lift force L per unit for a foil with no camber is:

$$C_L = \frac{L}{\frac{1}{2}\rho U^2 c} \approx 2\pi \sin \alpha \quad (27)$$

Where c is the chord length of the foil. For small angles, $\sin \alpha \approx \alpha$, so it reduces to:

$$C_L = \frac{L}{\frac{1}{2}\rho U^2 c} = 2\pi\alpha \quad (28)$$

Foils with camber have a lift force at $\alpha = 0$ which results in a relation of the form $C_L = 2\pi\alpha + C_{L_0}$.

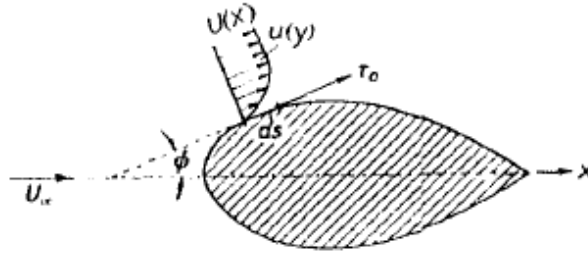


Figure 7: Skin friction due to laminar boundary layer [1].

Similarly, the 2D drag coefficient of a foil is defined as:

$C_D = \frac{D}{\frac{1}{2}\rho U^2}$, where drag force D is defined by its skin friction as seen in Figure 7.

3.4 Pressure Distribution

The pressure distribution on a foil is not uniform and it is due to pressure differences that separation can occur. As the angle of attack increases for a foil, the adverse pressure gradient increases [14]. It is important to note that a negative pressure gradient will counteract the retarding effect of the fluid due to viscosity and there will be no separation. Figure 9 shows typical pressure distributions of two foils at an angle of attack of $\alpha = 15^\circ$. Here, the non-dimensional pressure coefficient is used and is defined as:

$$C_p = \frac{p - p_0}{0.5\rho U^2} \quad (29)$$

where p_0 is the ambient pressure of the infinite fluid. At $\alpha = 0$ degrees, the stagnation points at the leading and trailing edge have negative C_p values. As α increases, the leading edge separation point moves downward to the bottom surface of the foil and the pressure on the top surface at the leading edge becomes larger, forming a significant peak. From these figures it is visible that the pressure on the top surface is more negative compared to the bottom, creating a resultant upward force that is the lift force.

3.4.1 Thickness Characteristics and 3D Effects

Thickness and 3D characteristics will influence the pressure distribution and ultimately separation. The foil to be tested is a standard NACA0025 foil, where the geometry of the upper side is determined by [15]:

$$y = \frac{5t}{c} (0.29690\sqrt{x} - 0.126x - 0.3516x^2 + 0.2843x^3 - 0.1015x^4) \quad (30)$$

Where t is the max thickness of the foil, which is $0.25c$. As there is no camber in this foil, the geometry is symmetric and the bottom side has a similar formula as Equation 30. The geometry of the foil is shown in Figure 8.

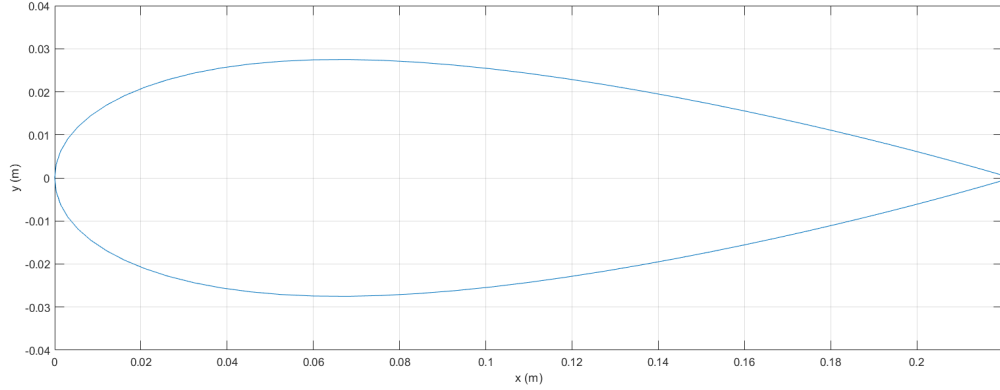


Figure 8: NACA0025 Profile

This particular foil is a relatively thick foil and its stall characteristics are shown in Figure 10 for three Reynolds numbers at which the hydrofoil will be tested. The advantage of thick foils over thin ones are its so-called "soft stall" characteristics. This means that the loss in lift for increasing angle of attack is gradual before dropping significantly, whereas a thinner foil will have a more abrupt loss of lift for higher angles of attack. This is due to the fact that boundary layer separation will occur at the leading edge for thinner foils, resulting in a fully turbulent wake instantly and significant loss of lift. For thicker foils, separation will occur more towards the trailing edge. This is shown in Figure 9, where a NACA0025 foil is compared to a NACA0012 foil at the same Reynolds number at an angle of attack of $\alpha = 15^\circ$. The thicker foil shows a delay in boundary layer separation compared to the thinner foil. As the angle of attack increases, the separation point moves towards the leading edge, eventually separating from the leading edge. This results in gradual loss of lift as opposed to a sudden drop of lift, as shown in Figure 10.

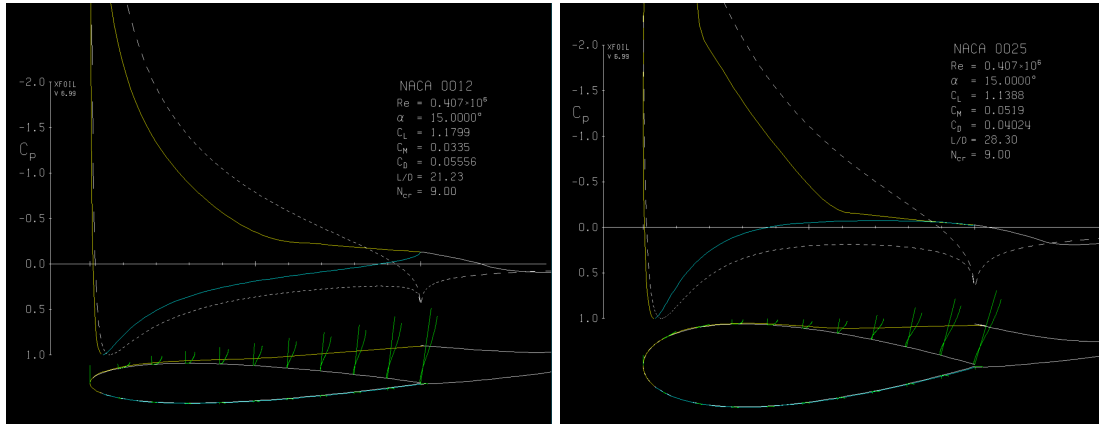


Figure 9: Boundary layer separation for two foils at $Re_2 = 4.070 \cdot 10^5$ and $\alpha = 15^\circ$. Derived from XFOIL [5].

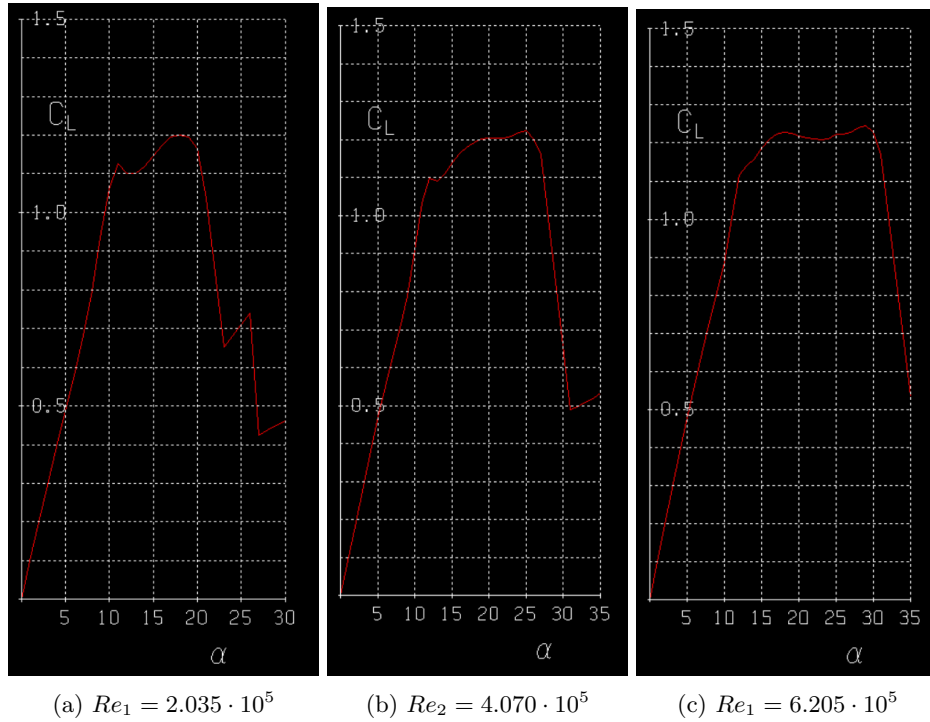


Figure 10: C_L as a function of α for NACA0025 for three Reynold's numbers. Derived from XFOIL.

These images are created by the software called XFOIL which calculates pressures, velocities and lift coefficients of 2D foils. XFOIL combines incompressible potential flow theory with viscous boundary layer formulation to calculate the values for boundary layers and wake through high-order panel methods for quick calculations [5]. As it is the simplified 2D case, we will expect

higher stalling angles due to 3D effects.

A 3D foil will have separation on the open end of the span, such as on the tip of an airplane wing, or on either side of a horizontal hydrofoil, for example. Both examples have a finite span and experience separation at those tips, where the flow will not be 2D. This has to do with the circulation of the flow around the foil. The flow 'wraps' around the tip due to the circulation and creates tip vortices. The circulation induces a downward velocity v called downwash, and reduces the angle of attack to an effective angle of attack, α_{eff} . As the effective angle of attack is smaller, it will reduce lift coefficient C_L . This in turn will delay the stalling region to a higher angle of attack compared to the 2D case. A large aspect ratio can help reduce 3D effects on a foil.

3.4.2 Pressure Gradients in Boundary Layer

If we take another look at the simplified boundary layer equations by Prandtl, Equation 6, we can make variables dimensionless with the characteristic length L of the object (e.g. for a foil, L would be the camber line c) and with the Reynolds number which is also characteristic of the object's length.

$$\begin{aligned}\bar{x} &= \frac{x}{L} & \bar{y} &= \frac{y}{L}\sqrt{Re} \\ \bar{u} &= \frac{u}{U} & \bar{v} &= \frac{v}{V}\sqrt{Re} \\ \bar{p} &= \frac{p}{\rho U^2}\end{aligned}$$

By substituting the above and inserting it in Equation 6, the simplified equation becomes [2]:

$$\bar{u}\frac{\partial\bar{u}}{\partial\bar{x}} + \bar{v}\frac{\partial\bar{u}}{\partial\bar{y}} = -\frac{\partial\bar{p}}{\partial\bar{x}} + \frac{\partial^2\bar{u}}{\partial\bar{y}^2} \quad (31)$$

Now, from the dimensionless variables, as \bar{y} remains constant, it can be seen that the thickness of the boundary layer, now y , is inversely proportional to the square root of the Reynolds number as seen before. The shape of the velocity profile is independent of the Reynolds number. The position of the laminar separation point, which is characterized by $\partial u/\partial y = 0$ at the $y = 0$, is independent of the Reynolds number. At $y = 0$, u and v both equal zero and Equation 31 becomes

$$\frac{\partial^2\bar{u}}{\partial\bar{y}^2} = \frac{\partial\bar{p}}{\partial\bar{x}} \quad (32)$$

When $\partial\bar{p}/\partial\bar{x}$ is positive (adverse pressure gradient), $\partial^2\bar{u}/\partial\bar{y}^2$ must also be positive and will result in a velocity profile as shown in Figure 11. Equation 32 also shows that when there is zero pressure gradient, e.g. a flat plate, the velocity profile is linear near $y = 0$. Figure 11 shows clearly that du/dy at $y = 0$ is larger for a positive pressure gradient than for a negative one.

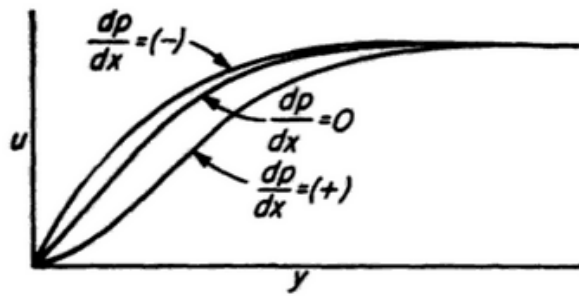


Figure 11: Influence of pressure gradient on velocity profile in the boundary layer [2]

Therefore it is clear to see that an adverse pressure gradient increases risk of separation as it increases the shear stress on the surface.

3.5 Examples in Practice

This section discusses two examples of skin friction reduction through alteration (modification) of the boundary layer. There are two main examples discussed, which is the practical application of air lubrication of ship hulls, and the other is the study of superhydrophobic surfaces.

3.5.1 Air Lubrication of Ship Hulls

Skin friction resistance is a very large resistance component of ships which accounts for approximately 60% to 80% of the total ship resistance [16]. Reducing skin friction resistance can therefore reduce emissions and fuel costs. To decrease the frictional resistance of a ship, Air Lubrication Systems (ALS) have been applied to ships which form a layer of very small bubbles below the hull, acting like a lubricated layer for the ship hull. An example is the Silverstream System, for which has been shown with in-service monitoring that it can actively reduce the frictional resistance up to 4% and predicts a reduction up to 8% [17]. Other ALS retrofits have shown a 4-5% net power saving for long in-service monitoring [16]. Another study estimated net energy savings of 10% to 20%, which correspond with Great Lake ship sea trials [6].

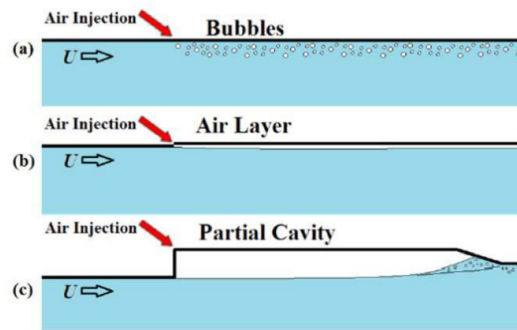


Figure 12: Three methods for air lubrication: (a) Bubble Drag Reduction, (b) Air Layer Drag Reduction, (c) Partial Cavity Drag Reduction. [6]

Figure 12 shows three different methods for air lubrication: bubble drag reduction, air layer drag reduction and partial cavity drag reduction. The purpose of these methods is that the air pockets remove the no-slip condition on the wall. The result is that the fluid has a velocity at the surface of the wall. This will be discussed in more detail in section 3.5.3.

3.5.2 Superhydrophobic Surfaces

Superhydrophobic surfaces are a different technique to reduce the skin friction of a surface. A superhydrophobic surface (SHS) has surface geometry that gives it water repellent characteristic and is defined by the angle between the edge of the water droplet to the horizontal at which a water droplet sits at rest, as sketched in Figure 13. This is called the (static) contact angle θ_c and must be larger than 150° for a SHS.

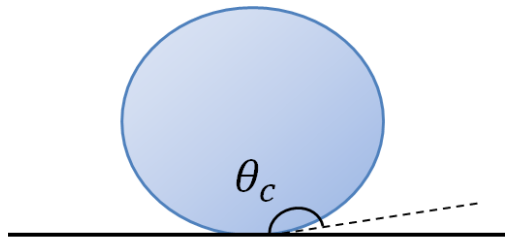


Figure 13: Contact angle for SHS

Figure 13 is a rough sketch of how the surface of a SHS actually looks. If we were to take a look at how the surface is in reality, we would see a rugged, or pinned, surface on which the water droplet rests.

There have been studies that show that SHSs successfully diminish the skin friction in laminar boundary layers [18]. Applying to turbulent boundary layers has not yet shown the same success, however.

3.5.3 Friction Reduction in Boundary Layers

When skin friction is reduced, it can remove the no-slip condition that was previously on the surface and create what is called a "partial slip" condition. Subsequently, the water has a velocity at the wall called the slip velocity, denoted as u_s . The slip velocity can be defined as:

$$u_s = u(y = 0) = \lambda \left(\frac{du}{dy} \right) \Big|_{y=0} \quad (33)$$

Where λ is the slip length. Instead of a velocity profile as shown in Figure 2 the velocity profile now looks like the one sketched in Figure 14 where the velocity at the wall depends on the slope of the velocity change in y at the wall. The slope du/dx below $y = 0$ is assumed to be linear.

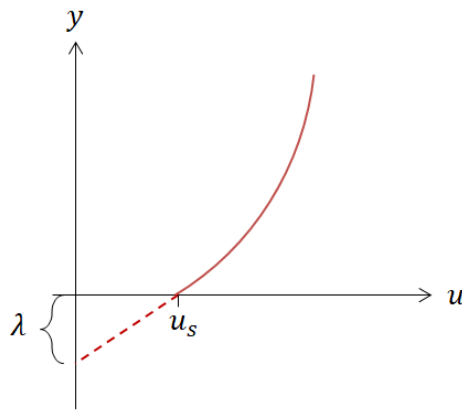


Figure 14: Slip condition for friction reduction surfaces

4 Foil Prototype Design

To investigate the boundary layer, inspiration was taken from a hydrofoil designed by Juan Francisco Fuentes-Perez at the Technical University of Tallinn (TalTech), shown in Figure 15. This NACA-based foil called iRon is initially used for research of local velocities and pressures on the surface of fish with use of six differential pressure sensors. It was proposed to use this prototype for this research, as the pressure sensors could be useful to investigate details of the boundary layer. Furthermore, a foil has a relatively stable (and known) separation region. However, after further consideration, it seemed that iRon was not quite suitable to measure the boundary layer due to the fact the pressure sensors were only positioned near the leading edge of the foil. For details of the boundary layer, a better picture of the pressure distribution over the chord length is needed. A new foil prototype was designed and subsequently built at the Center for Biorobotics Laboratory at TalTech in Tallinn, Estonia.

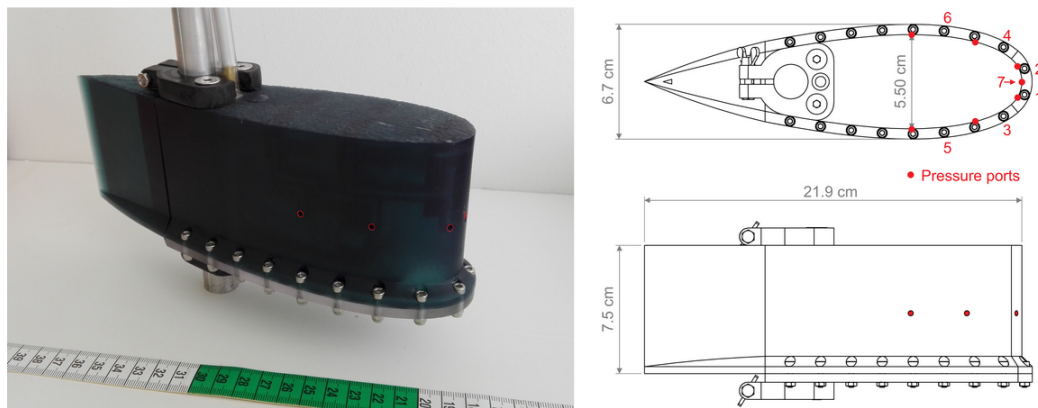


Figure 15: Design of the iRon foil prototype [7]

4.1 Detailed Design

The new design is based much on the original design of iRon. Figures 16 and 17 show the main dimensions of the prototype. Figure 16 shows the prototype without top clamp while figure 17 shows the top view with the clamp. The clamp is fixed on top of the foil in Figure 19, and the end result looks like Figure 21. The foil is designed in 3D CAD software called Solidworks. The foil parts are 3D printed by Formlabs 2 printer, with Formlabs' tough resin. Information about the resin can be found in Appendix C. The foil and electrical components are constructed by Juan Francisco Fuentes-Pérez.

The top of the foil is slightly widened, as can be seen in Figure 16, so that the top clamp can cover all the electronics inside. The clamp is placed at its center of pressure, which is at $0.25c$ from the leading edge for symmetric foils: $c/4 = 55 \text{ mm}$. This is the origin for the x and y forces, as seen in Figure 24.

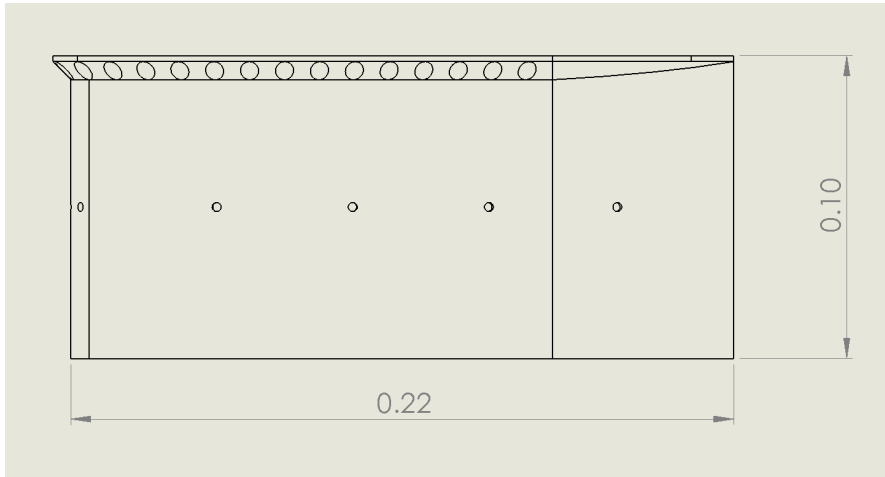


Figure 16: Side view without clamp. Dimensions in *m*.

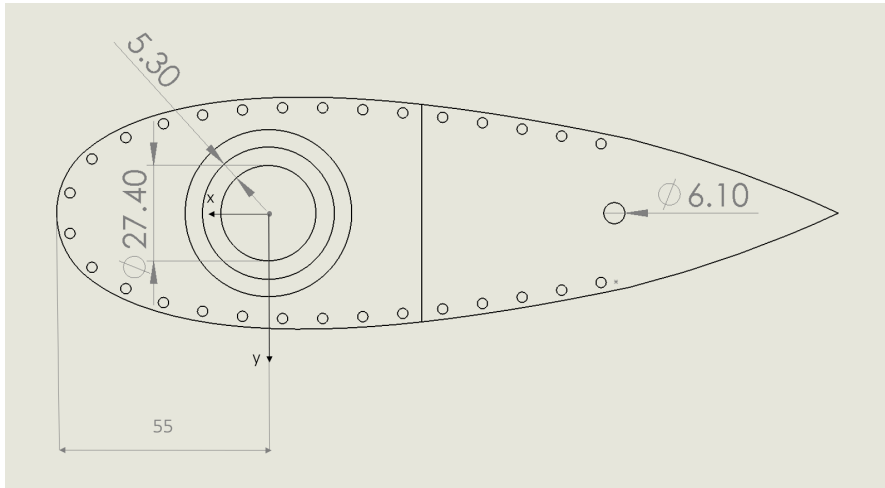


Figure 17: Top view with clamp. Dimensions in *mm*.

There are ten MPXV7002 differential pressure (DP) sensors equipped in the foil and one MPX5010G absolute pressure sensor. The DP sensors measure the difference in pressure between two adjacent holes on a single side of surface of the foil, ranging from -2000 to 2000 Pa. These holes can be seen in Figures 16 and 18. The sensors are placed on each side of the foil and the holes are (symmetrically) spaced 45 mm apart over the chord length, the last hole being 1 mm closer to the second last than the rest, shown in Figure 18. There are eleven holes on the surface and Figure 19 gives an indication of the layout of the holes and the relation to the sensors. Sensor 11 (henceforth written as s11) is the absolute pressure sensor and is connected to the far most left hole seen in Figure 18, which is placed at the very tip of the leading edge on the chord line of the foil, i.e. the foil's center line. Sensor 1 (s1) is connected to this hole and the adjacent hole, the second from the left in figure 18, indicated as 1 in Figure 19. Sensor 3 is connected to holes indicated as 1 and 3 in Figure 19, s5 is connected to holes 3 and 5, and so forth. This is

shown in Table 1 and the corresponding midway points along the chord are given. Note that this is identical for the opposite side for the even-numbered sensors. Each hole is therefore shared by two adjacent sensors, apart from the most left hole in Figure 18 which is shared by two DP sensors and one absolute pressure sensor. Figure 20 shows s9 (in black) and how it is connected to two adjacent holes and also shows some additional tubing of the foil. More information about the MPXV7002 DP sensors can be found in Appendix A.

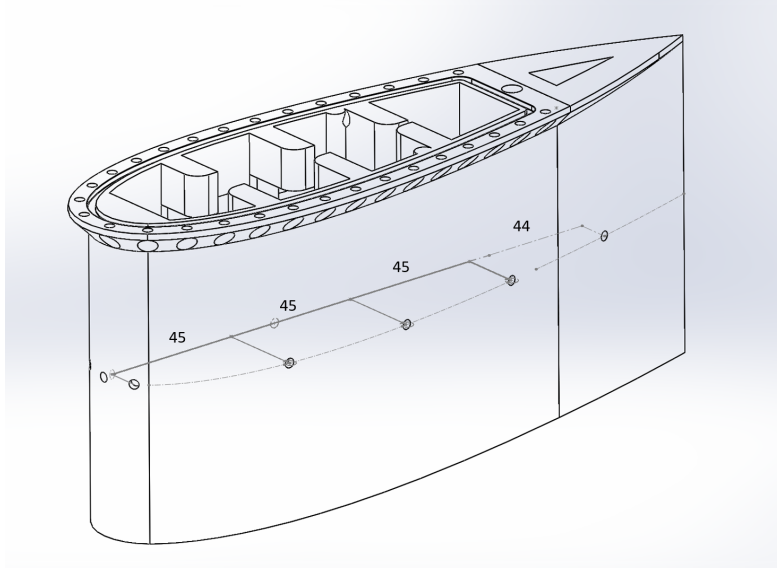


Figure 18: Distance between the pressure holes on the chord line in *mm*.

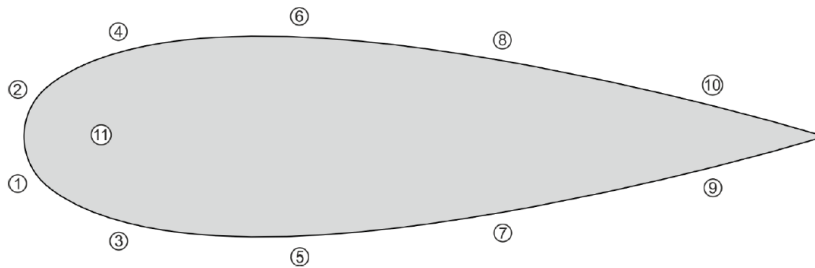


Figure 19: Layout of the holes. Courtesy of Juan Francisco Fuentes-Pérez (Appendix B)

Sensor	Hole No.	x/c	x (mm)
1	11-1	0.011	2.50
3	1-3	0.114	25.0
5	3-5	0.3182	70.0
7	5-7	0.523	115
9	7-9	0.0723	159

Table 1: Sensors and their corresponding measuring points including the midway point on chord between the sensor's holes.

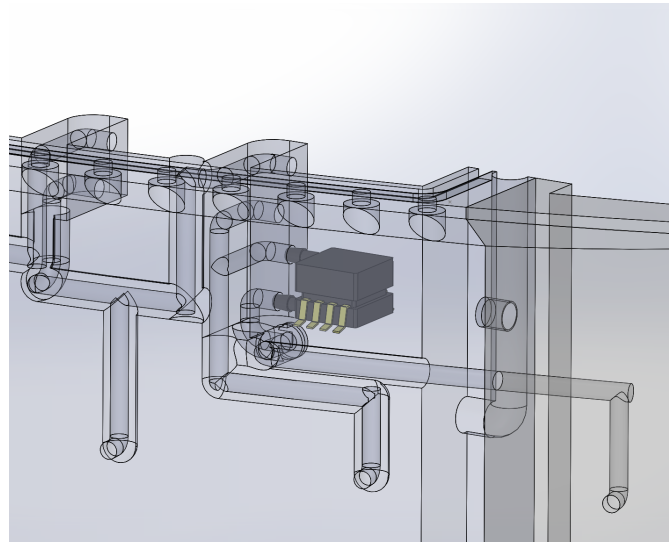


Figure 20: Section half of the foil with s9 and the foil's tubing structure. Holes 5, 7 and 9 are shown.

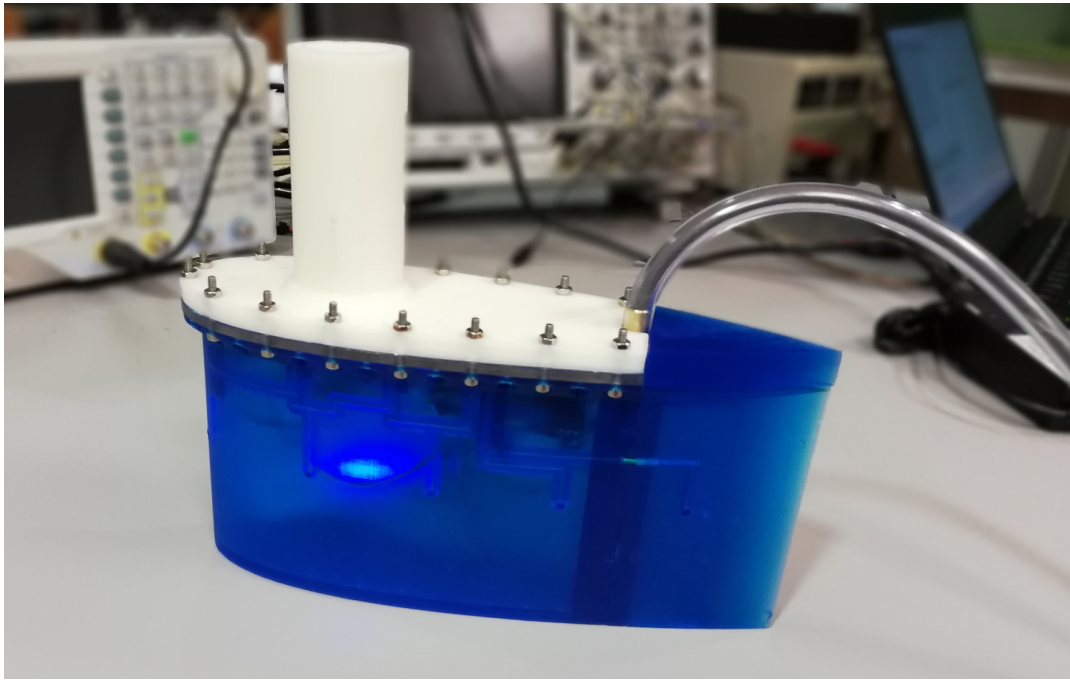


Figure 21: Finished prototype. Courtesy of Juan Francisco Fuentes-Pérez.

5 Experimental Setup

This section gives a description of the experimental setup in the towing tank for testing the hydrofoil. An overview of the test runs and conditions are given and the anti-fouling coating is described in detail. During the tests we experienced leaking problems, preventing further testing. This is explained in more detail.

5.1 Test Setup

Tests were performed at the towing tank in Sintef Ocean in Trondheim. The total length of the towing tank is 260m and the towing tank has two carriages. Only part of the total basin is used for the tests, which is 175m long. The width is 10.5m and the depth is 5.6m [19].

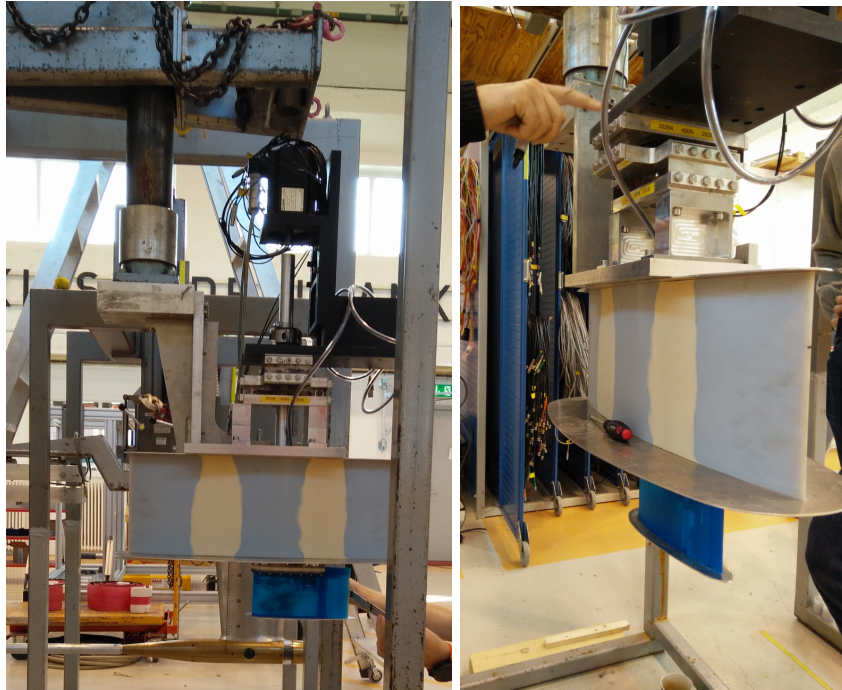


Figure 22: Foil set up in the rig

The top clamp of the foil is attached to a vertical metal cylinder with a length of 1m, which is attached to a force gauge measuring x and y forces experienced by the foil. The force gauge can be seen right below the black metal part of the rig shown in Figures 22 and 26. The foil is placed underneath a larger, surface-piercing foil equipped with a relatively large end plate to diminish free-surface effects as much as possible. Ideally, the prototype foil should be flush with the bottom of the end-plate. However, as the USB cable sticks out from the top of the prototype, a gap between the top of the prototype foil and the water-piercing foil cannot be avoided. The USB cable was carefully bent and held in place by a zip-tie to close the gap as

much as possible, resulting in a 2.5 cm gap. Furthermore, the screws on top of the foil also prevent a flush connection, but in the end the USB cable was the limiting factor, as seen in Figure 25. It is important for the tests that the USB cable does not touch the bottom of the end-plate as this could influence the forces measured on the foil. Figure 23 shows a sketch of the rig setup in the tank. The distance between the bottom of the surface-piercing foil and the prototype foil is 13.5 cm . The distance between the top of the surface-piercing foil and the water surface is 11 cm .

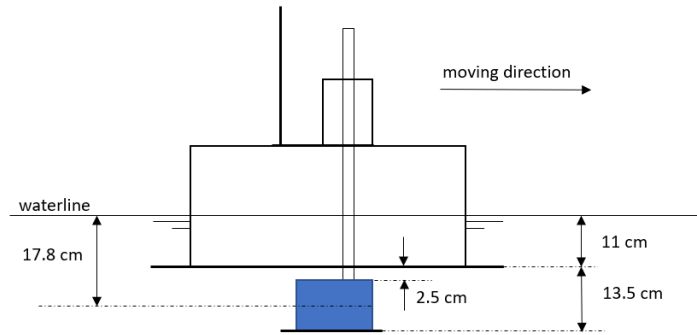


Figure 23: Sketch of the test setup in the water.

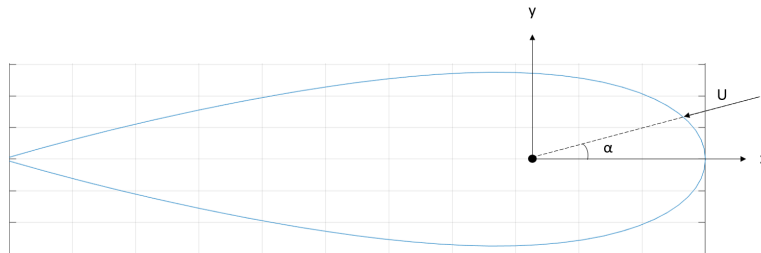


Figure 24: Definition of positive angle of attack.

The rig is set up such that the angle of attack can easily be changed by rotating the cylinder to which the foil is attached, without changing the height of the foil relative to the rig, as seen in Figure 26. The angle of attack is measured by an angle wheel seen in Figures 27 and 26 where a pin soldered to a clamp indicates the angle. The angle must be adjusted by hand and measured by eye and therefore accuracy is estimated to be about $\pm 1^\circ$. Positive angles are defined as in Figure 24. This means that for positive angles, the even-numbered sensors are on the suction side.

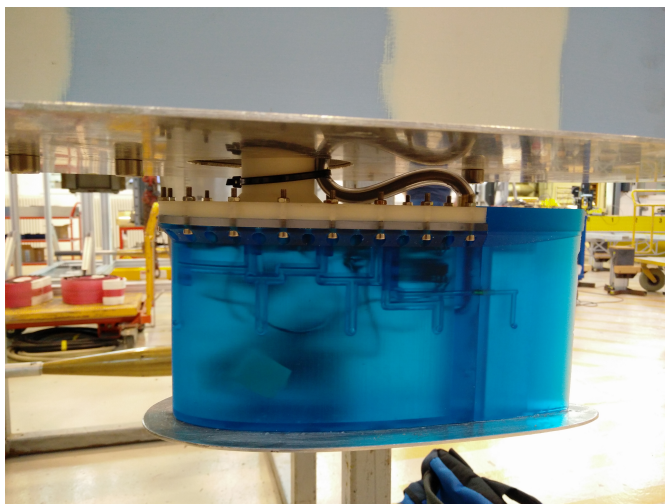


Figure 25: Gap between surface-piercing foil and the prototype.

5.2 Test Conditions

5.2.1 Test Runs

The towing tank is long enough to complete three velocity measurements in a single run, so for every set angle of attack, the forces and pressures are measured at constant speeds of $u_1 = 1 \text{ m/s}$, $u_2 = 2 \text{ m/s}$, and $u_3 = 3 \text{ m/s}$, which correspond to Reynolds numbers shown in Table 2. Here, the kinematic viscosity is $\nu = 1.0811 \cdot 10^{-6} \text{ m}^2/\text{s}$ [20], determined by the average temperature of 17.05°C , which was averaged over a single run in the towing tank. The kinematic viscosity ν is assumed constant for every other run.

u (m/s)	Re
1	$2.035 \cdot 10^5$
2	$4.070 \cdot 10^5$
3	$6.105 \cdot 10^5$

Table 2: Speeds tested with corresponding Reynolds numbers

Force and pressure measurements are carried out for at least 10 s per speed run to reach steady state conditions and the carriage accelerates at $a = 0.6 \text{ m/s}^2$ when advancing to the next speed. Each angle of attack is repeated twice or three times to get more accurate pressure averages. Table 3 shows all the runs carried out for the foil, first two days of testing an uncoated foil and then another day of testing after the foil was coated in anti-fouling paint. More information about the paint is given in section 5.2.2. The runs are indicated by a small code to refer to them easily, containing the angle and run number. For example, run 251 indicates the first run of $\alpha = 25^\circ$, and run 252 indicates the second run of $\alpha = 25^\circ$. For the coated foil, the code contains

the number 3 in front of the angle and run number, to indicate that these are runs of the third (and coated) day. Run 3302 represents the second run of angle $\alpha = 30^\circ$.

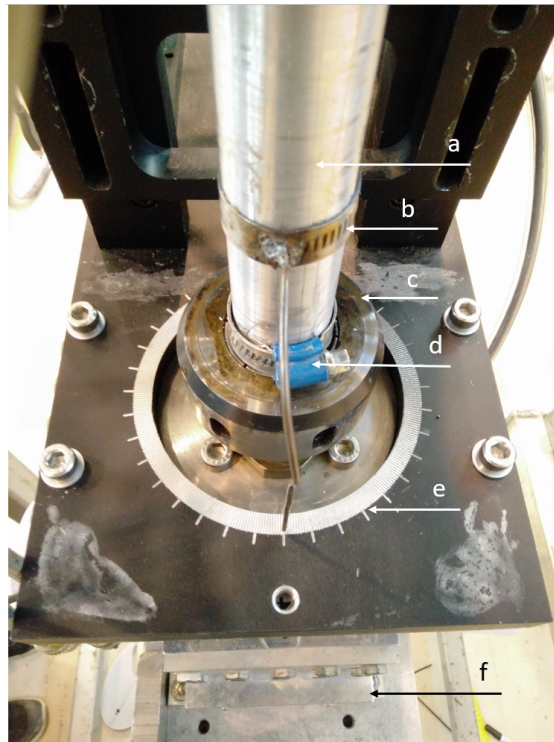


Figure 26: a) cylinder fastened to foil clamp. b) angle indicator. c) clamp holding cylinder in place. d) ensures cylinder does not fall when clamp c is loosened. e) angle wheel. f) force gauges.

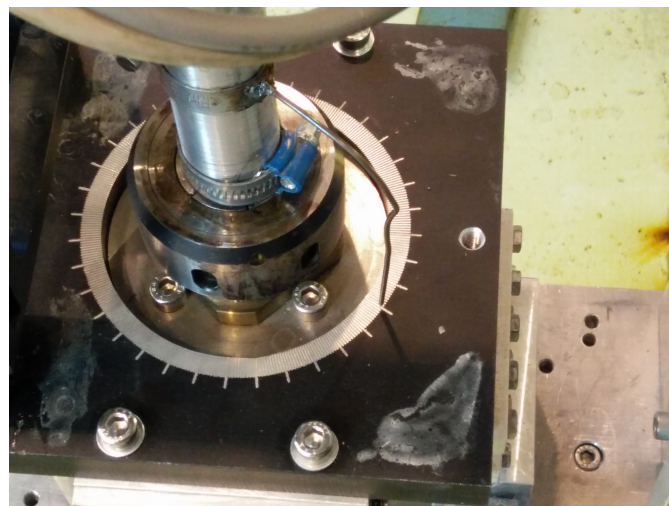


Figure 27: Angle wheel indicating the angle of attack

<i>Uncoated foil</i>						<i>Coated foil</i>		
day 1			day 2			day 3		
run	angle (deg)	no.	run	angle (deg)	no.	run	angle (deg)	no.
001	0	1	281	28	1	3001	0	1
002	0	2	282	28	2	3002	0	2
101	10	1	238	28	3	3281	28	1
102	10	2	321	32	1	3282	28	2
103	10	3	322	32	2	3301	30	1
151	15	1	323	32	3	3302	30	2
152	15	2	331	33	1	3321	32	1
153	15	3	332	33	2	3331	33	1
201	20	1	333	33	3	3332	33	2
202	20	2	351	35	1	3333	33	3
251	20	3	352	35	2	3351	35	1
252	25	1	353	35	3	3352	35	2
253	25	2	m321	-32	1	3353	35	3
254	25	3	m322	-32	2			
301	30	1	m201	-20	1			
302	30	2	m202	-20	2			
303	30	3						

Table 3: All runs for the three test days with the uncoated and coated foil

5.2.2 Anti-Fouling Coating

The second series of tests has been carried out with the coated foil. The anti-fouling coating has been applied by the Jotun paint company in Sandefjord and consists of three layers. Below, the product name and description of all three layers are given [21].

1. **N10:** Two-component polyamine cured pure epoxy coating. It is a high solid, high build, abrasion resistant product. Specially designed as a universal, all round, all year, new building coating where fast dry to handle is required. Can be used as primer, mid coat, finish coat or as single coat system in atmospheric and immersed environments. Suitable for properly prepared aluminium, carbon steel, galvanised steel, shop primed steel and stainless steel substrate. It can be applied at sub zero surface temperatures.
2. **SeaQuest Tiecoat:** Three component elastomeric silicone tie coat. Provides adhesion between the SeaQuest silicone topcoat and the primer. Based on polysiloxane.
3. **SeaQuest:** Three-component elastomeric silicone fouling release coating. It is biocide free and provides effective fouling protection and hull performance. This is achieved by a

smooth, low friction surface reducing hull deterioration. This is to be used as finish coat in immersed environments and is polysiloxane based.



Figure 28: Coated foil with rough edges around the sensors' measuring points.

While the coating should provide reduced skin friction, the three layers that make up the coating are very thick. This makes the holes on the side of the foil stick out from the surface much more than before, instead of being completely flush with the surface. The edges were cut down and smoothed out as much as possible to make the surface flush with the holes, but it was challenging, as the layers are thick and the paint is quite brittle. After cutting and smoothing, the holes' edges remained rough, as shown in Figure 28. To get an idea of the difference in skin friction, the C_D forces for zero angle of attack are compared in Table 4.

5.3 Leaking Problems

The original goal was to repeat all measurements from day 1 and 2 listed in Table 3 with the coated foil. However, after receiving the coated foil from Sandefjord, the internal electronics connected to the pressure sensors were not working, indicating an initial leak in the foil. After inspection, it appeared that the rubber O-ring under the cover may not have sealed completely, causing a bit of leakage (about half a cm in the foil) that had caused corrosion of the electronics. The foil was opened and the lab technicians from Sintef Ocean cleaned the electronic components and re-soldered the wires.

After soldering, the electronics worked again and the foil was put back together with a thicker O-ring. Unfortunately the screws were screwed on too tight while putting it back together and caused some cracking of the holes. This in turn caused the foil to leak a lot once it was submerged, and the foil completely filled with water. In a last attempt to get some readings, we dried the components again, and put it back together with a lot of silicone sealing to ensure

water tightness. However, after about 13 runs on the carriage, connection was lost again and the foil had filled with water completely. Water may have gotten through the USB pipe this time, as the top cover still seemed sealed water tight with the silicone. The cover was removed once more and the electronics were dried and cleaned. However, setting up more time for testing in the towing tank was not an option anymore. As seen in Table 3, only six different angles were measured with the coated foil.



Figure 29: Waterlogged foil.

6 Results

This section gives analyses of the measured forces and pressures by looking the lift and drag forces and comparing them to the coated foil. Differential pressure distributions are plotted over chord length with standard deviations, to see how the boundary layer develops. These are also compared to the coated foil, and some insight is given through the differential pressure signals. The repeatability of the sensors is discussed shortly and a spectral analysis is made to see if vortex shedding can be identified.

Forces and pressures are measured simultaneously during a run but are not measured by the same device. The force transducer is connected to Sintef Ocean computers on board the carriage, while the pressure sensors are connected to my personal laptop. The measurement runs are timed to start and stop at the same time to the best of our ability. However, this means that the runs are not perfectly synchronized; there is some human error involved. This is not a problem for the average values used.

6.1 Force Analysis Uncoated

The lift and drag forces on the foil are measured during the runs to find the stall angles. Figure 30 and Figure 31a show the mean of three runs of lift and drag coefficients for angles 0° to 35° for all three Reynolds numbers.

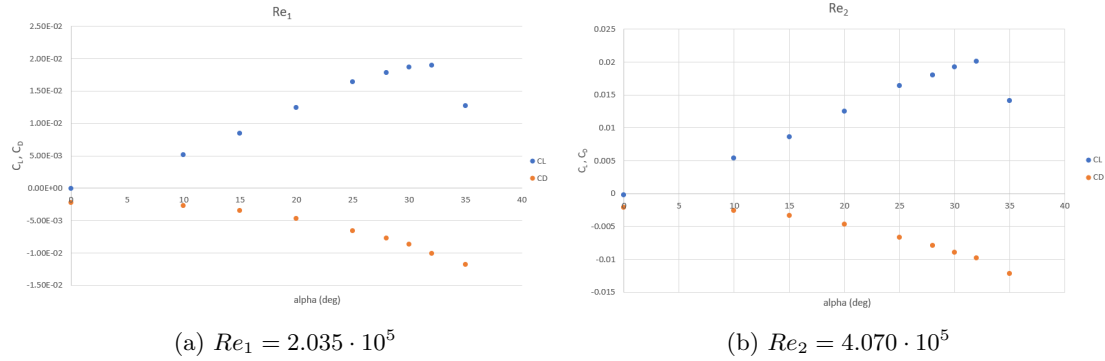
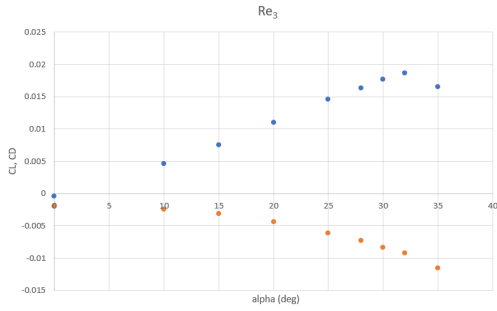
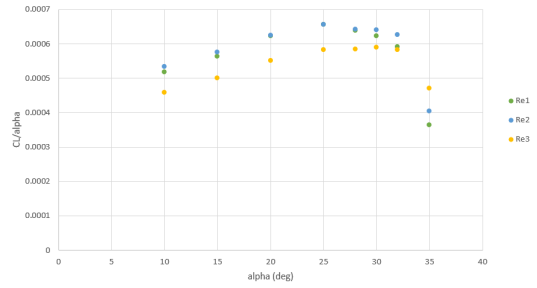


Figure 30: Mean C_L and C_D as a function of α .

Here, we notice significant difference with Figure 10. In all three cases, the hydrofoil stalls at a higher angle than in the 2D case, which is due to 3D effects. What is also noticeable is that the lift coefficient tends to drop more sudden than in the 2D case, meaning it has lost a bit of its soft stall characteristics as seen in Figure 10. The lift drops significantly at 35° , although at around $\alpha = 28^\circ$ (or slightly higher), the lift coefficient curve gives a good indication that the foil is losing lift. A sudden and significant drop in lift could indicate separation from the leading edge due to the 3D effects. The 3D characteristic might prevent separation anywhere else on the foil except from the leading edge. For Re_3 , the drop in lift coefficient is less significant than for the other two Reynolds numbers.



(a) Mean C_L and C_D as a function of α for Re_3



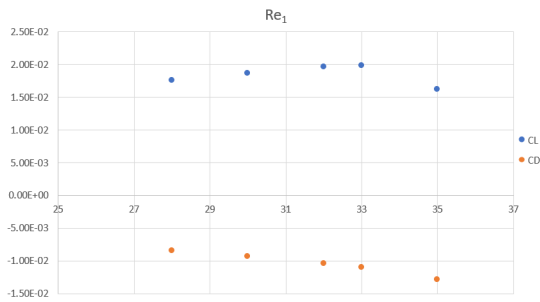
(b) C_L/α as a function of α

Figure 31: a) Force coefficients for Re_3 and b) C_L/α as a function of α for three Reynolds numbers.

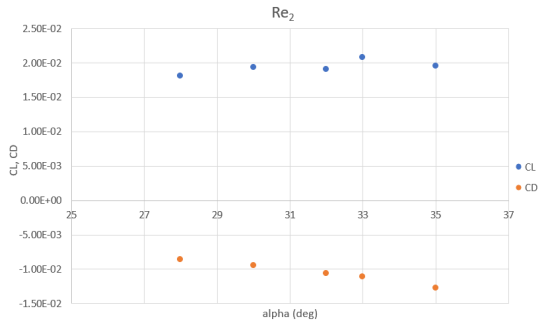
Figure 31b shows how C_L changes over α . This is overall largest for Re_2 and lowest for Re_3 . It is clear from Figures 30 and 31a that the stalling region is at $\alpha > 32^\circ$. The region in between $\alpha = 28^\circ$ and $\alpha = 35^\circ$ is therefore important for boundary layer development and separation which is where we will direct our attention to try to observe these phenomena. An angle of 32° or 33° seems on the verge of complete separation.

Over all angles, the lift coefficient is generally highest for Re_2 and lowest for Re_3 . At 35° , Re_1 has the lowest lift coefficient.

6.2 Force Analysis Coated



(a) Mean C_L and C_D as a function of α for Re_1



(b) Mean C_L and C_D as a function of α for Re_2

Figure 32: Mean C_L and C_D as a function of α for two Reynolds numbers for the coated foil.

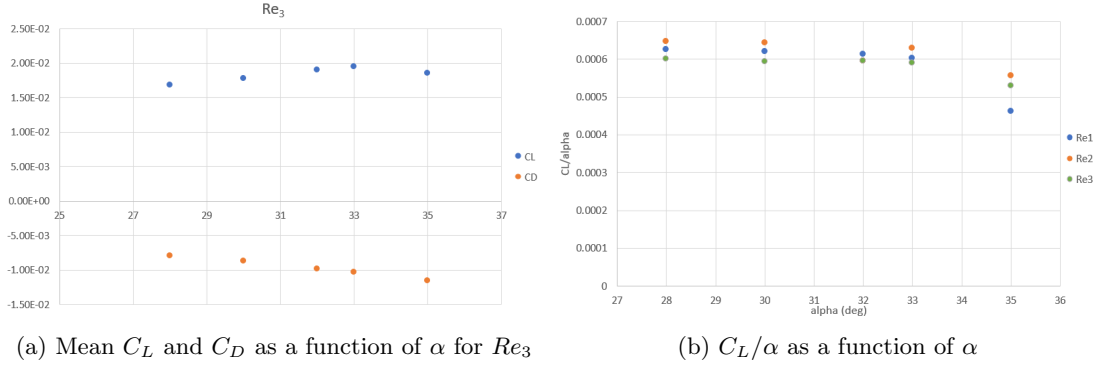


Figure 33: a) Force coefficients for Re_3 and b) C_L/α as a function of α for three Reynolds numbers for coated foil.

The maximum C_L for the coated foil has increased for every Reynolds number compared to the uncoated foil. The maximum has also shifted from $\alpha = 32^\circ$ to $\alpha = 33^\circ$, where it seems now the foil will stall for $\alpha > 35^\circ$, whereas for the uncoated foil stalls for $\alpha > 32^\circ$. Maximum magnitude of C_D at 35° has increased for the coated foil. Overall, the drag force is larger for the coated foil than for the uncoated foil.

A higher drag is also seen at $\alpha = 0^\circ$, where we would expect a decrease in drag for the paint, shown in Table 4. So even though the drag increased with the paint, the coating results an overall delay in stall.

	Average C_D		
	Re_1	Re_2	Re_3
uncoat	-0.00221	-0.00215	-0.00199
coated	-0.00264	-0.00248	-0.00225

Table 4: Average C_D for $\alpha = 0^\circ$ for uncoated and coated foil.

6.3 Differential Pressure Distributions

Considering how the foil is built and the location of the pressure sensors, the pressure coefficient defined as in Equation 29 cannot easily be used with the obtained differential pressures. Instead, a differential pressure coefficient is used, defined as Equation 35. Imagine two points on the surface of the foil, point 1 and point 2. The difference in pressure will be:

$$dp = p_2 - p_1 \quad (34)$$

$$dC_p = \frac{dp}{0.5\rho U^2} = \frac{p_2 - p_1}{0.5\rho U^2} \quad (35)$$

Where U is the free stream velocity.

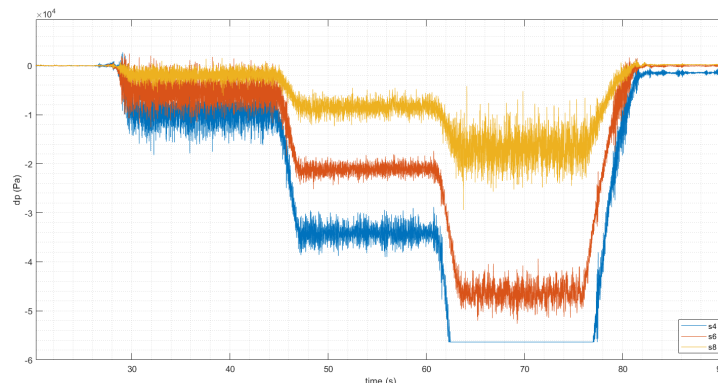


Figure 34: Run 1201 with the signals of three pressure sensors on the suction side.

Figure 34 shows the signals of s4, s6 and s8 for run 201 ($\alpha = 20^\circ$) with the mean zero-speed value subtracted. Every run starts at u_1 and goes up to u_3 in step wise manner before ending the run, where the signals on the suction side decrease step wise for every step higher in speed (pressure signal increases in magnitude). We notice that the signal is more negative as we get closer to the leading edge, as expected. In fact, s2 is already oversaturated at u_2 , so that one is left out. Oversaturation can be seen in the figure for s4 at u_3 . Unfortunately, oversaturation happens quite fast for s2 and s4 (similar for s1 and s3 for negative angles).

For processing the data, the zero speed value of every signal is averaged and subtracted from the original signal. Then, every signal is split into its three velocity components and divided by $\frac{1}{2}\rho U^2$ to get dC_p . Then, with dC_p known, the average dC_p value and standard deviation for every velocity can be found.

Every run is repeated at least twice, with the exception of run 3321 due to that the foil was waterlogged, to get a better estimation of the average dC_p values. The standard deviation σ of C_p for a given run gives an indication of the relative pressure fluctuations and therefore gives an indication of unsteady (chaotic) flow.

6.3.1 Uncoated

Figures 35 to 39 show the absolute mean differential pressure distributions as a function of chord length for angles $\alpha = 15^\circ$ to $\alpha = 35^\circ$ and for the two negative angles. The standard deviation for every signal is also plotted. Although the standard pressure distribution cannot be plotted over the chord length, it is interesting and helpful to see how the differential pressure behaves as a function of chord length. It is a way to compare all runs with each other and will show how dC_p changes with angle, Reynolds number and chord length.

For every angle of attack, the pressure peak $dC_{p,max}$ decreases with increasing Reynolds number. This could indicate a more constant pressure distribution for higher Reynolds numbers. It is

noticeable that in most cases, $dC_{p,max}$ is found at or near the leading edge and that the difference in pressure coefficient reduces over the chord length further away from the leading edge.

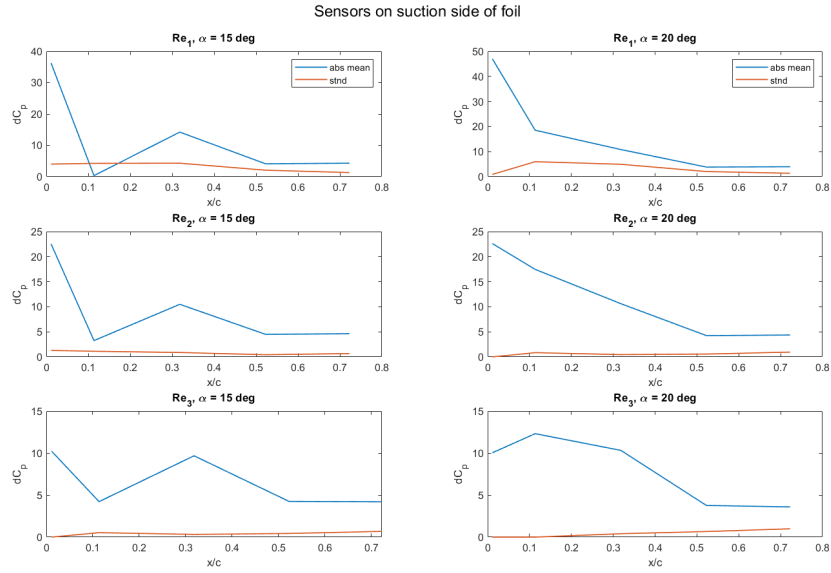


Figure 35: Mean differential pressure distribution and standard deviation over chord length for $\alpha = 15^\circ$ and $\alpha = 20^\circ$.

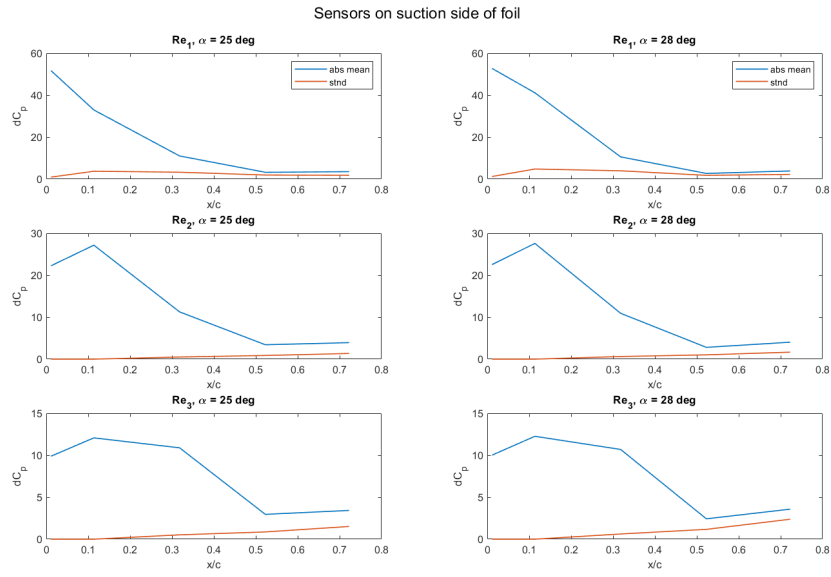


Figure 36: Mean differential pressure distribution and standard deviation over chord length for $\alpha = 25^\circ$ and $\alpha = 28^\circ$.

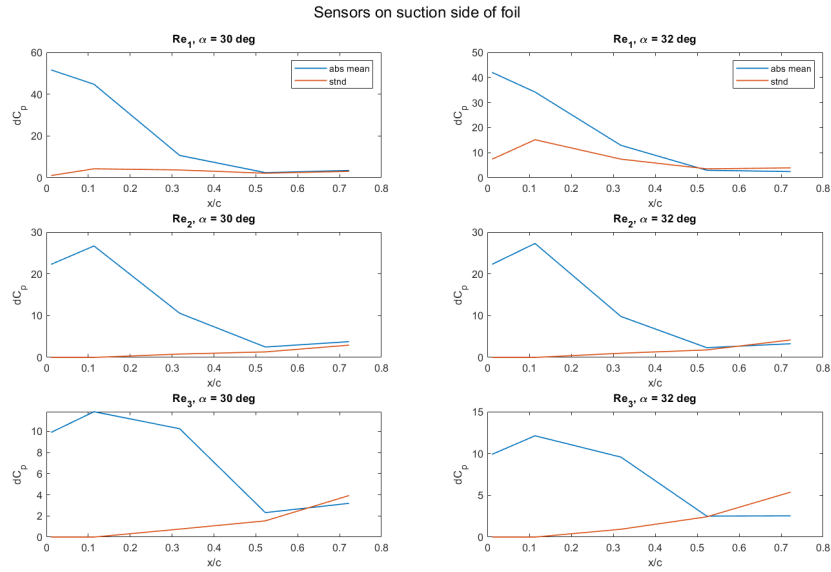


Figure 37: Mean differential pressure distribution and standard deviation over chord length for $\alpha = 30^\circ$ and $\alpha = 32^\circ$.

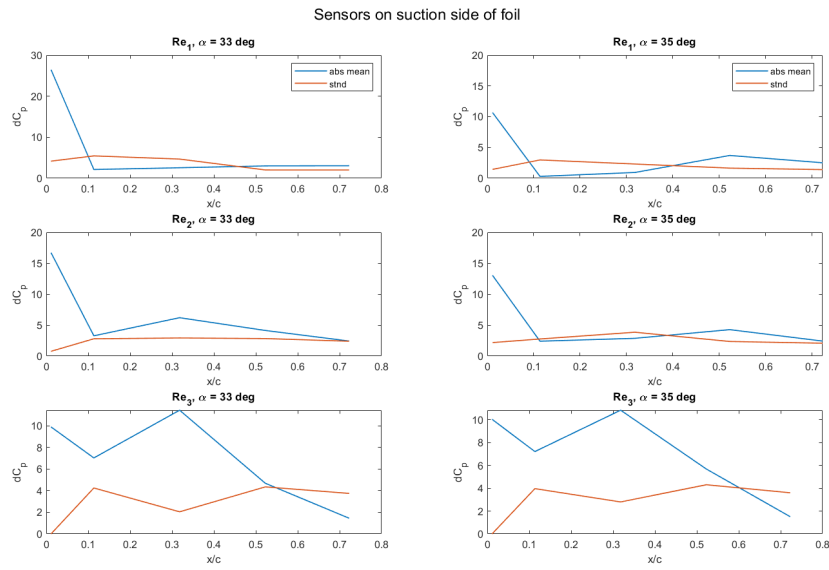


Figure 38: Mean differential pressure distribution and standard deviation over chord length for $\alpha = 33^\circ$ and $\alpha = 35^\circ$.

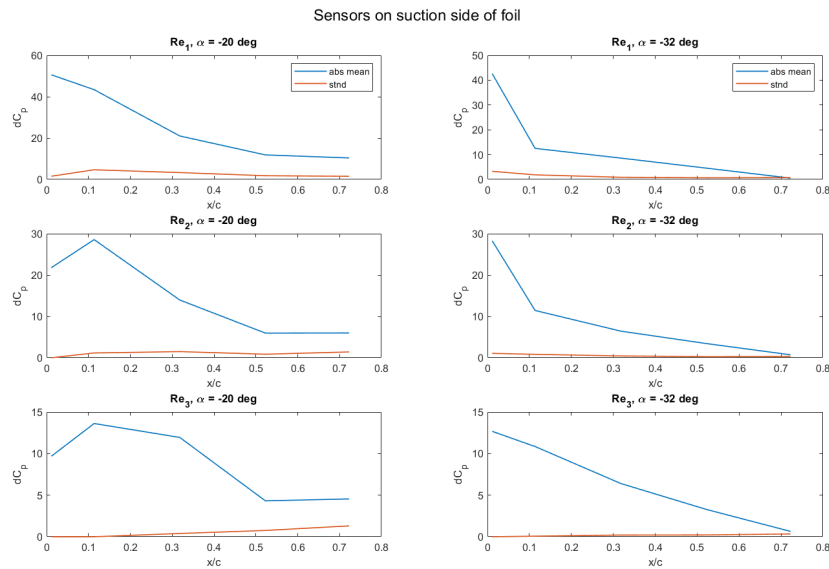


Figure 39: Mean differential pressure distribution and standard deviation over chord length for $\alpha = -20^\circ$ and $\alpha = -32^\circ$.

Overall, the standard deviation increases over chord length, more significantly for higher angles

($\alpha \geq 25^\circ$). Standard deviation increases much more significantly for high Reynolds numbers and high angles ($\alpha \geq 30^\circ$), which could be explained by turbulent flow due to flow separation. This would be in agreement of a developing, and eventually separating boundary layer.

Figure 40 shows the average standard deviation of C_p as a function of the angle for all the sensors. A standard deviation of $\sigma = 0$ indicates an oversaturated sensor. Fluctuation peaks up to $C_p = 15$ can be found for Re_1 for the front sensor. Overall, the standard deviation increases with increasing angle, The peaks can be found around $\alpha = 32^\circ$ for all three Reynolds numbers and diminishes at $\alpha = 35^\circ$, where we would expect a more unsteady flow due to separation.

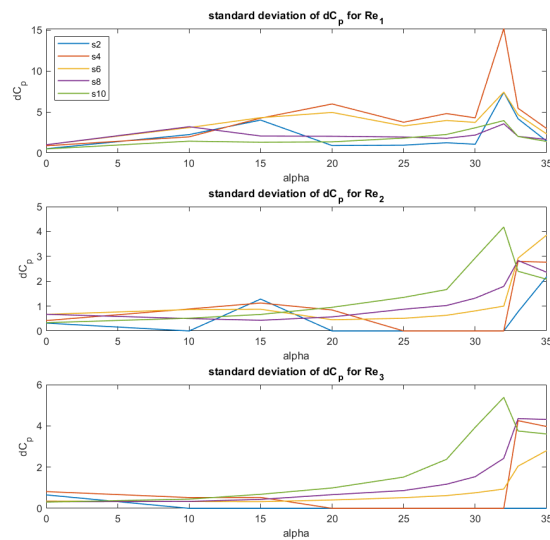
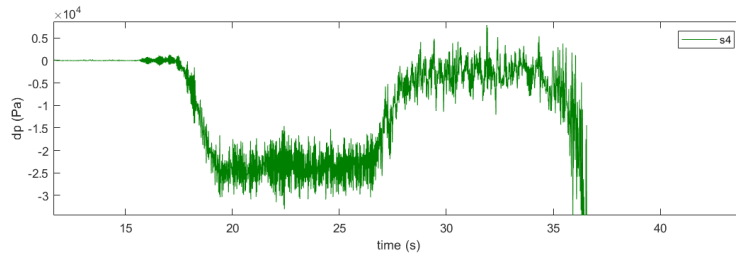
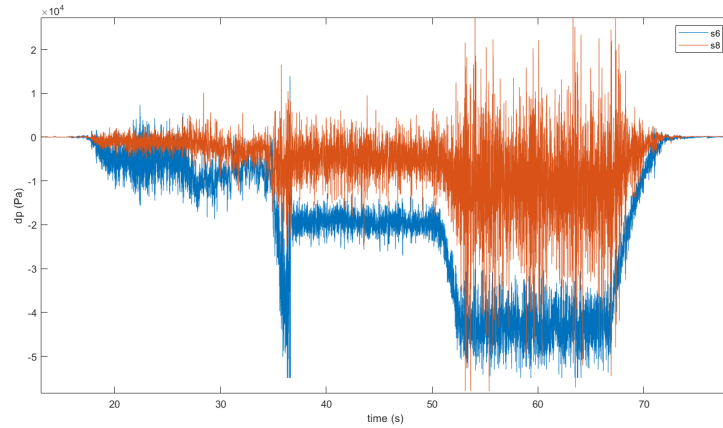


Figure 40: Standard deviation of C_p averaged over all runs as a function of α for all sensors for three Reynolds numbers.

Figure 37 shows a spike for the standard deviation near the leading edge for Re_1 . It is worth looking into, so the time series for the dp signal is shown in Figure 41. Sensors 6 and 8 are plotted for the whole run in Figure 41b, in which a significant transient period can be observed after going from u_1 to u_2 . The average signal was carefully taken after the transient region in the steady-state region. Moreover, a strange development can be observed throughout u_1 , especially noticeable for s6. This region is highlighted in 41a for s4. This is indeed a strange and sudden jump in pressure.



(a) sensor 4 shown only during speed u_1



(b) sensor 6 and 8 shown for full run

Figure 41: Time series of dp signals for run 322.

Looking at the F_L and F_D force signals in Figure 42, there seems to be a jump in fluctuation after $t \approx 28s$. The mean lift force decreases from $9.78 N$ from $t = 22s$ to $28s$ to $8.52 N$ for $t = 28s$ to $33s$ and the standard deviation for those two time periods is $\sigma_L = 2.16 N$ to $\sigma_L = 4.51 N$, respectively. Loss in lift and increase in fluctuation could very well indicate separation between hole 2 and 4. Similarly, we would expect an increase in drag force. Mean drag force goes from $-4.95 N$ to $-5.41 N$ and the standard deviation goes from $\sigma_D = 1.73 N$ to $\sigma_D = 3.80 N$ for their respective time periods. Thus, drag force increases in magnitude as expected. Run 323 shows a similar situation.

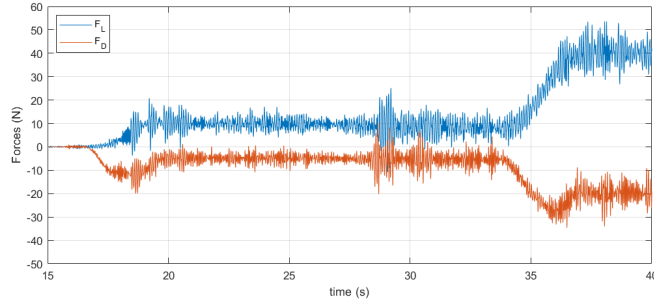


Figure 42: Time series of force signals for run 322 during u_1 .

The same jump in pressure is seen at 35° at Re_2 (i.e., during the u_2 run) in Figure 43 for s4, where the jump is significant. The fluctuations also become much larger after this jump, which happens at about $t = 44$ s. In fact, this jump in pressure can also be seen on the sensor on the opposite side, s3, which has also been plotted. The lift force on the foil makes a significant jump as well, as seen in Figure 44. Here, the run for u_1 and u_2 can be seen. The jump happens also at around $t = 44$ s during the u_2 velocity run, although this time the lift increases. For the two time periods during u_2 , $t = 38$ – 44 s and $t = 46$ – 53 s, the mean lift force goes from $F_L = 26.4$ N to $F_L = 35.4$ N, while $\sigma_L = 4.57$ N and $\sigma_L = 5.72$ N, respectively. The mean drag force goes from $F_D = -24.1$ N to $F_D = -24.4$ N, and the standard deviation goes from $\sigma_D = 3.84$ N to $\sigma_D = 4.77$ N. So in this case, the drag force hardly changes and the lift force increases, while both standard deviations increase. This could possibly be caused by reattachment, although that would not yet explain the increase in fluctuation after this point.

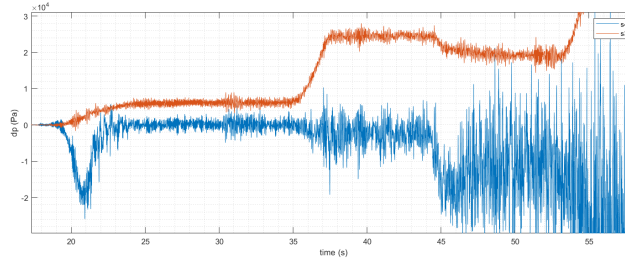


Figure 43: Time series of dp signals for run 352.

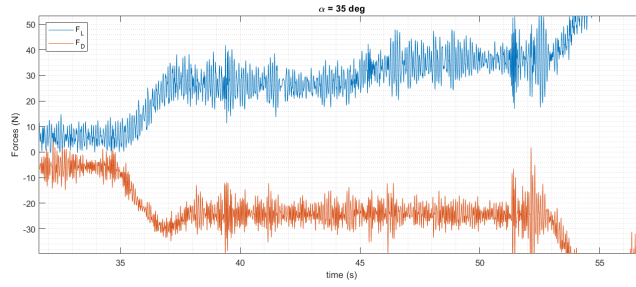


Figure 44: Time series of force signals for run 352.

6.3.2 Comparison of Coated and Uncoated Data

Figures 45, 46 and 47a show that for angles of $\alpha \leq 30^\circ$, the differential pressure distribution is in relative good agreement for the uncoated and coated foil, with the maximum difference ranging up to approximately 20% for 28° and 30° . For 32° , the difference in dC_p goes up to approximately 30%, while for 33° and 35° the values vary enormously. The reason for this difference in behaviour can likely be attributed to stalling occurring at around 33° for the uncoated foil, while the coated foil does not exhibit significant loss in lift at even 35° .

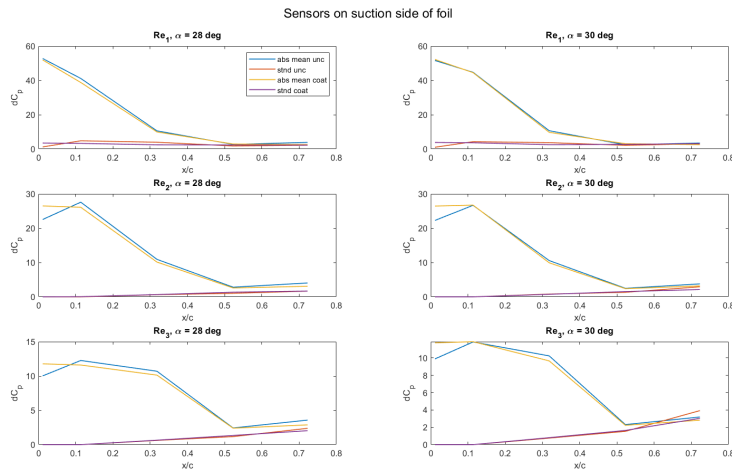


Figure 45: Comparison of differential pressure distribution over chord length for $\alpha = 28^\circ$ and $\alpha = 30^\circ$ for uncoated and coated foil.

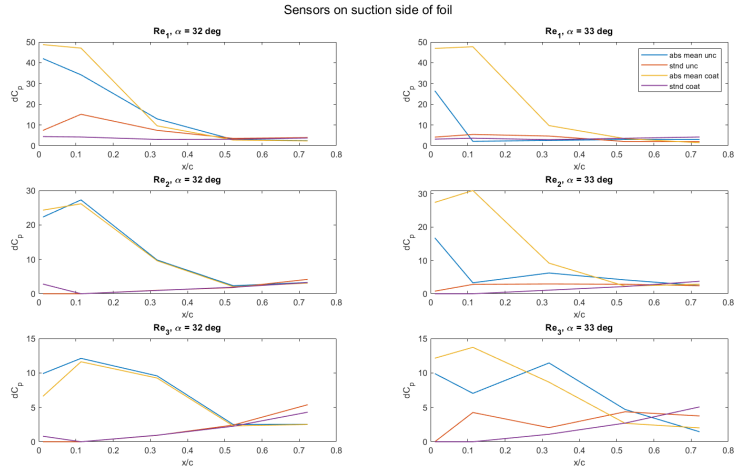
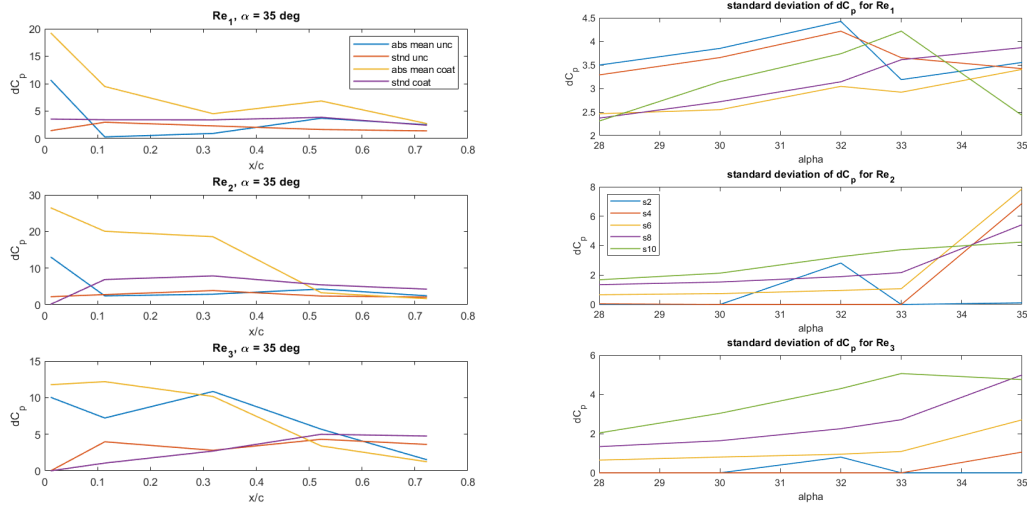


Figure 46: Comparison of differential pressure distribution over chord length for $\alpha = 32^\circ$ and $\alpha = 33^\circ$ for uncoated and coated foil.



(a) Comparison diff. pressure dist for $\alpha = 35^\circ$ (b) standard dev as a function of α for coated foil

Figure 47: Comparison of differential pressure dist for $\alpha = 35^\circ$ standard deviations of sensors as a function of α for coated foil.

So for higher angles, i.e. $\alpha > 32^\circ$, we notice for the coated foil a differential pressure distribution that starts out large and diminishes somewhat smoothly over the chord length, whereas the uncoated foil has significant drops or spikes in differential pressure coefficient, noting that stalling occurs around 33° for the uncoated foil. The coated differential pressure profile for 33° is more comparable to the differential pressure profile of 32° for the uncoated foil. In most cases, the

standard deviation over the chord length is smaller for the coated foil than for the uncoated foil, meaning less unsteady flow in these regions. The standard deviation for Re_2 and Re_3 increases with angle for the coated foil, seen in Figure 47b, while for Re_1 the peaks are around 32° and 33° , like the uncoated foil. This could indicate that the stalling region for the coated foil is for $\alpha > 35^\circ$.

6.3.3 Precision of the Pressure Sensors

It's hard to get an accurate picture of the repeatability, because there are maximum three runs for a given angle. Figure 48 shows the differential pressure coefficient as a function of chord for three runs with their respective means. The runs for $\alpha = 25^\circ$ are so close to one another, that the graph had to be zoomed in a lot to see differences between the runs. This is different for a stalling angle of $\alpha = 33^\circ$, where there is much fluctuation in the runs. To get a better picture of run differences, the standard deviation of the mean values of each angle are plotted for sensors 2, 4, 6, 8, and 10, shown in Figure 49 and Figure 50.

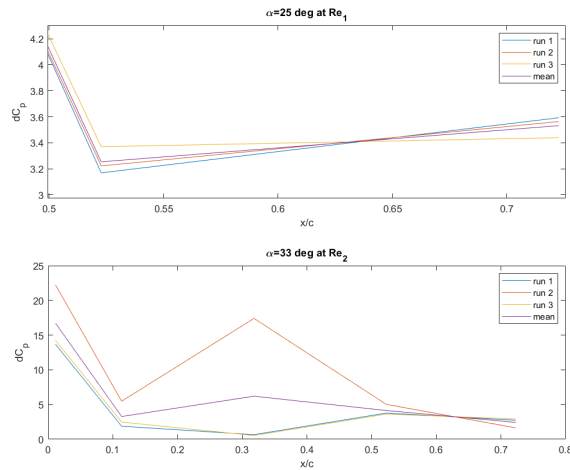


Figure 48: Two examples of repeated runs and their mean.

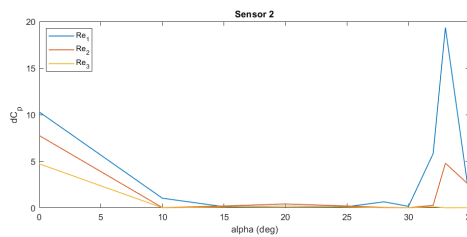


Figure 49: Standard deviation of all runs combined as a function of alpha for sensor 2.

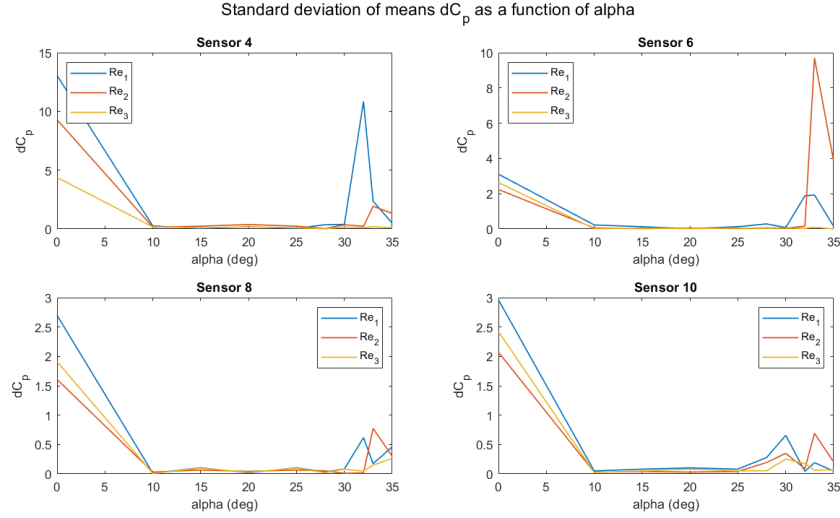


Figure 50: Standard deviation of all runs combined as a function of alpha for four sensors.

At zero degrees, the standard deviation is relatively large and decreases to almost zero at 10° and until approximately $\alpha = 32^\circ$ does not fluctuate nearly as much as at zero degrees. This is due to the difference in runs for 0° is large for its mean value and fluctuations are relatively large for low angles compared to their mean value, but are not large for higher angles, where the mean value is larger. Large peaks can be seen at 32° and 33° , meaning that the velocity runs are spread out from each other at these angles. One would need many repetitions for these angles to get an accurate value.

6.4 Frequency Analysis

In stall conditions at high angles we expect vortex shedding from the hydrofoil. The separation does not have to occur from a single point. In fact, we can expect oscillating vortices from the leading and trailing edge, as we would have on either sides of a cylinder in steady high Reynolds flow (Figure 5). Like the cylinder, the lift and drag forces might be influenced by the shedding vortices, which will then result in oscillations of the forces. The vortex shedding frequencies can be calculated. For the foil, the projected Strouhal number is used as defined by C. Sarraf, *et al* [8] as Equation 36. So instead of a fixed Strouhal number as in equation 26, the Strouhal number is now also a function of α . A frequency analysis is done on the force signals to see whether it is possible to identify the given frequencies from Table 5.

$$St = \frac{f_v}{U} c \sin \alpha \quad (36)$$

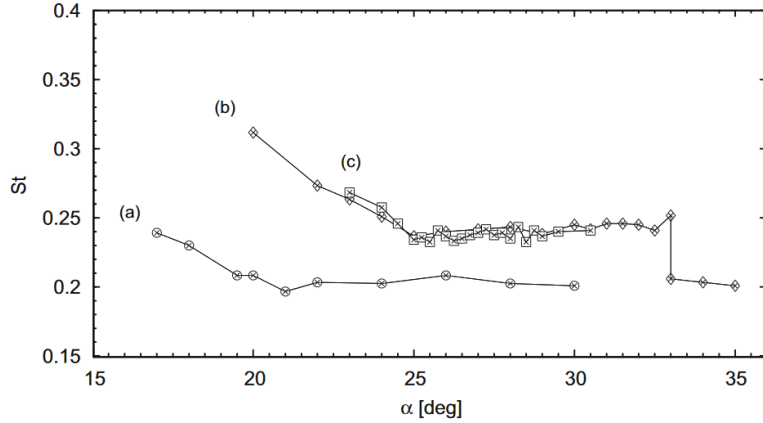


Figure 51: Strouhal number as a function of alpha at $Re = 5 \cdot 10^5$ for three profiles: (a) NACA0015, (b) NACA0025 and (c) NACA0035. [8]

To find the vortex shedding frequencies at a certain angle of attack, the Strouhal number for a given angle is taken from Figure 51, which shows the Strouhal number for various angles of attack for a NACA0025 foil. For the tested angles, we would expect oscillations of the lift force close to those listed in Table 5. The Reynolds number from where the Strouhal numbers are taken from is $Re = 5 \cdot 10^5$, which is in between Re_2 and Re_3 for the tests.

α (deg)	d (mm)	St	f_v (Hz)
0	0	-	-
10	38.2	-	-
15	56.9	-	-
20	75.2	0.31	37.45
25	93.0	0.24	23.47
28	103	0.25	22.00
30	110	0.25	20.66
32	117	0.25	19.49
33	120	0.26	19.73
35	126	0.20	14.41

Table 5: Projected Strouhal number (Eq. 36) for angles of attack from Figure 51 and their corresponding vortex shedding frequencies. Distance $d = c \sin \alpha$.

Figures 52, 53 and 54 show the spectral density of the lift force signal as a function of frequency for angles 25, 30, 33 and 35 degrees. Figure 53 also includes the drag force signal. For every spectrum, the frequencies between 10 and 12 Hz have a large peak, as well as a significant peak in the area of 25 Hz. The fact that these frequencies are generally present for all angles, makes it likely that in the 10-12 Hz range, it is noise due to vibrations of the carriage or test rig, for

example. In most cases, Re_3 contains the larger peaks in the spectrum, except for $\alpha = 33^\circ$. The main peaks for Re_3 are generally spaced closer together than for Re_2 .

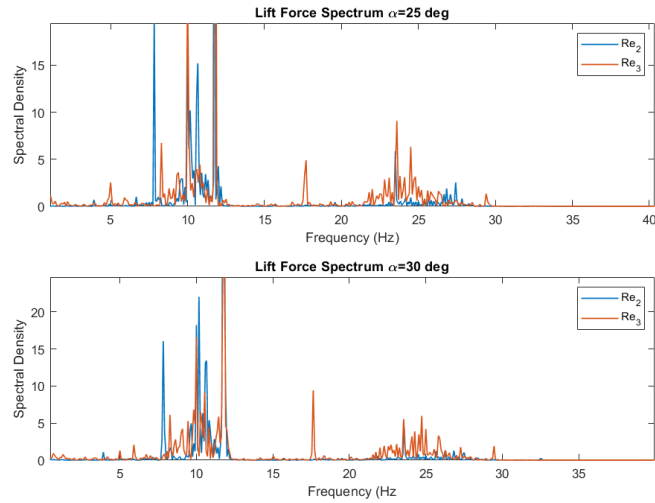


Figure 52: Spectral density of lift as a function of frequency for various 25 and 30 degrees.

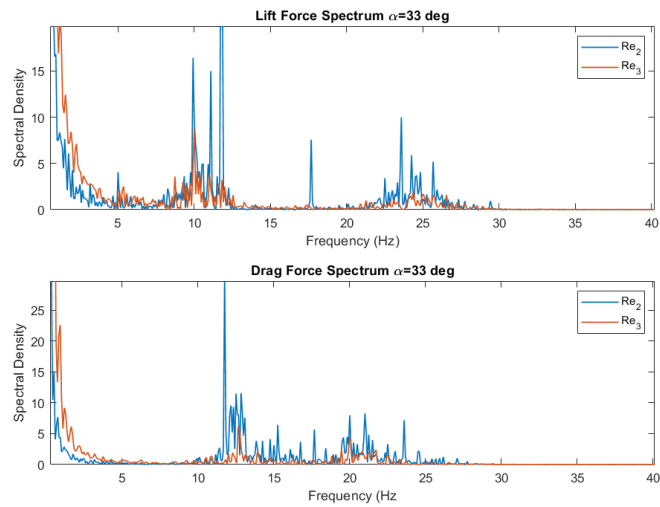


Figure 53: Spectral density of lift and drag as a function of frequency for 33 degrees.

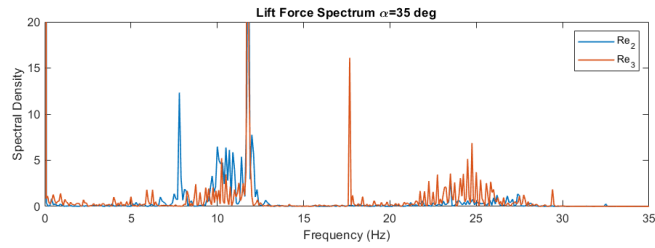


Figure 54: Spectral density of lift force signal as a function of frequency for $\alpha = 35^\circ$

For these angles, hardly any correlation can be found with the vortex shedding frequencies in Table 5, except for $\alpha = 25^\circ$, where a definite peak can be found at 23 Hz, which could be related to the unsteady flow. Note also that the frequency contents in this range is different for the lift force than for the drag force, which further suggests this is linked to flow processes and not to carriage vibrations. For the drag frequencies in Figure 53, we would expect large peaks at double frequencies from lift which are 10–12 Hz and 23–26 Hz. There are peaks present at 20–24 Hz that do not contain much energy which may be attributed to vortex shedding. Frequencies above 40 Hz are nonexistent.

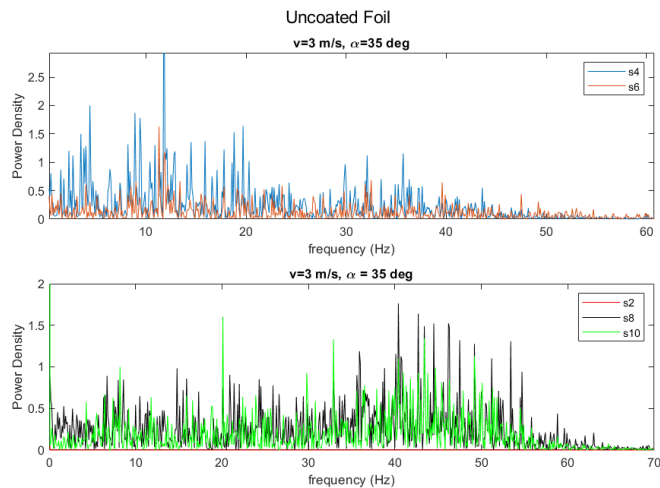


Figure 55: Spectral density of sensor signals as a function of frequency for $\alpha = 35^\circ$

To see if the frequency spectrum from the force signal corresponds with any of the sensors, a power density spectrum is made at $\alpha = 35^\circ$ shown in Figure 55, noting that the uncoated foil is experiencing stall in these conditions, so that noise in the pressure fluctuations can be expected. Here, there also seems a large peak at around 12 Hz for s4. The spectra for s8 and s10 seem to have a large amount of energy at higher frequencies, in between 35 and 55 Hz. It is clear that more needs to be investigated into the nature of the frequencies for the pressure sensors to be able to conclude anything from the power spectra.

7 Discussion

The 3D effects were very large. Even though we expected higher angles of stall, this stalling region was higher than expected, and more abrupt. With more time, higher angles could have been included in the tests. Perhaps with higher angles of attack, alternate vortex shedding would have been easier to detect.

Although the runs were supposed to have been stationary, there still seemed to be surprising jumps in pressure during a constant velocity run once in a while, which may be attributed to boundary layer separation/reattachment. However, it is possible this was a mistake in the rig, where the foil perhaps turned due to high forces. After investigation into the rig and clamp, this was dismissed. This could be checked with more repetitions.

Higher drag of the coated foil is an unexpected result. It is possible that this is due to the rough holes of the pressure sensors, or may just be characteristic of the paint, that will wear off over time during further use.

The repeatability of the pressure sensors was hard to determine with limited number of runs, and therefore also difficult to compare with one another. Especially for the higher angles, the results vary greatly. Oversaturation for some of the sensors occurred more often than expected, which made some of the data difficult to analyze.

8 Conclusions and Recommendations

8.1 Conclusions

Force measurements are done to find the stalling regions of the uncoated and coated foil. Due to 3D effects, stall is observed at around $\alpha = 33^\circ$ for the uncoated foil and the drop in lift is more abrupt than in the 2D case. For the coated foil, maximum lift coefficient is higher than for the uncoated foil and the stalling region is delayed, stalling at $\alpha > 35^\circ$. Overall, lift coefficient is increased with the anti-fouling coating, while drag coefficient is increased. The drag is increased by the anti-fouling paint.

For every angle of attack, the pressure peak $dC_{p,max}$ decreases with increasing Reynolds number. This could indicate a more constant pressure distribution for higher Reynolds numbers. For the coated foil, the standard deviation increases over chord length, more significantly for higher angles ($\alpha \geq 25^\circ$). Standard deviation increases much more significantly for high Reynolds numbers and high angles ($\alpha \geq 30^\circ$), which could be explained by turbulent flow due to flow separation. This would be in agreement of a developing, and eventually separating boundary layer. The exact point of separation could not easily be observed. This may in part be due to oversaturation of sensors. The differential pressure distribution in combination with the standard deviation can indicate whether a foil is stalling.

For angles $\alpha > 32^\circ$, we notice for the coated foil a differential pressure distribution that starts out large and diminishes somewhat smoothly over the chord length, whereas the uncoated foil has significant drops or spikes in differential pressure coefficient, noting that stalling occurs around 33° for the uncoated foil. The coated differential pressure profile for 33° is more comparable to the differential pressure profile of 32° for the uncoated foil. In most cases, the standard deviation over the chord length is smaller for the coated foil than for the uncoated foil, meaning less unsteady flow in these regions. The standard deviation for Re_2 and Re_3 increases with angle for the coated foil, while for Re_1 the peaks are around 32° and 33° , like the uncoated foil. This suggests that the stalling region for the coated foil occurs at an angle $\alpha > 35^\circ$.

A frequency analysis shows that for $\alpha = 25^\circ$, a definitive peak can be found at 23 Hz, which could be related to the unsteady flow. The frequency content in this range is different for the lift force than for the drag force, which further suggests this is linked to flow processes and not to carriage vibrations. For the drag force frequencies in Figure 53, we would expect large peaks at double frequencies from lift which are 10–12 Hz and 23–26 Hz. There are peaks present at 20–24 Hz which may be attributed to vortex shedding. Frequencies above 40 Hz, in the region of $2f_v$ are nonexistent. For $\alpha = 35^\circ$ there also seems a large peak at around 12 Hz for s4, though most sensors give a lot of noise making the reading difficult. It is clear that more needs to be investigated into the nature of the frequencies for the pressure sensors to be able to conclude anything from the power density spectra.

8.2 Recommendations for Further Work

Though the differential pressure sensors were hard to analyze, there is a lot of potential in these sensors taking the sensitivity into account. With a higher pressure range, the sensors would have

been able to measure much more at the leading edge of the foil. These sensors would work better for lower Reynolds number. Another option is to place the holes on the surface and on a point in the freestream velocity, so that the actual C_p can be measured. To continue using this foil, one might need to look into making the holes more flush with the surface and making them less rough around the edges.

As the 3D effects were very significant, a much larger aspect ratio for a foil is recommended. A lifting line code should be made to estimate the effect of the 3D shape, so that stalling region can be predicted beforehand. It is helpful to measure up to higher angles of attack.

Differences in boundary layer are hard to observe on a small foil like this, for future boundary layer analyses, I recommend a more reliable setup in a cavitation tunnel, where high Reynolds flows can be created in a stable environment. One could observe boundary layer development on a flattened surface, where the development is more gradual and a longer distance than the chord length of a foil. This would be helpful for a superhydrophobic surface. A test setup where boundary layer separation can be observed easily is highly recommended.

The results from this research project suggest that coating a foil with a hydrophobic anti-fouling paint could shift the occurrence of stalling towards higher angles of attack. The potential relevance for marine vehicles should be evaluated further.

9 References

- [1] Hermann Schlichting and Klaus Gersten. *Boundary-Layer Theory*. Springer Berlin Heidelberg, Berlin, Heidelberg, 9th ed. 2017 edition, 2017.
- [2] Ira H Abbott. Theory of wing sections : including a summary of airfoil data, 2012.
- [3] Frank M White. Viscous fluid flow, 2006.
- [4] Odd M Faltinsen. Sea loads on ships and offshore structures, 1990.
- [5] M. Drela. XFOIL. <http://web.mit.edu/drela/Public/web/xfoil/>, 2013. Accessed: 26-01-2019.
- [6] Brian R. Elbing, Simo Mäkiharju, Andrew Wiggins, Marc Perlin, David R. Dowling, and Steven L. Ceccio. On the scaling of air layer drag reduction. *Journal of Fluid Mechanics*, 717(2012):484–513, 2013.
- [7] M. J. Costa, J. F. Fuentes-Perez, I. Boavida, J. A. Tuhtan, and A. N. Pinheiro. Fish under pressure: Examining behavioural responses of iberian barbel under simulated hydropeaking with instream structures.(research article)(report). *PLoS ONE*, 14(1), 2019.
- [8] C. Sarraf, H. Djeridi, S. Prothin, and J.Y. Billard. Thickness effect of naca foils on hydrodynamic global parameters, boundary layer states and stall establishment. *Journal of Fluids and Structures*, 26(4):559–578, 2010.
- [9] F.E. Fish and G.V. Lauder. Passive and active flow control by swimming fishes and mammals. 38(38):193–224.
- [10] ERIK J. ANDERSON, WADE R. MCGILLIS, and MARK A. GROSENBAUGH. The boundary layer of swimming fish. *Journal of Experimental Biology*, 204(1), 2001.
- [11] Juan F Fuentes-Perez, Kaia Kalev, Jeffrey A Tuhtan, and Maarja Kruusmaa. Underwater vehicle speedometry using differential pressure sensors: Preliminary results. In *2016 IEEE/OES Autonomous Underwater Vehicles (AUV)*, pages 156–160. IEEE, 2016.
- [12] James W Gose, Kevin Golovin, Mathew Boban, Joseph M Mabry, Anish Tuteja, Marc Perlin, and Steven L Ceccio. Characterization of superhydrophobic surfaces for drag reduction in turbulent flow. 845:560–580, 2018.
- [13] P. W. ; Collicott Steven H. ; Valentine Daniel T. Houghton, E. L. ; Carpenter. *Aerodynamics for Engineering Students*. Elsevier Science, 6 edition, 2012.
- [14] Zifeng Yang, Fred Haan, Hui Hu, and Hongwei Ma. An experimental investigation on the flow separation on a low-reynolds-number airfoil. In *45th AIAA aerospace sciences meeting and exhibit*, page 275, 2007.
- [15] National advisory committee for aeronautics. <https://web.archive.org/web/20090427002114/http://www.fges.demon.co.uk/cfd/naca.html#07>. Accessed: 11-03-2019.
- [16] Jaedoo Lee V, Jungjoong Kim, Booki Kim V, Jinho Jang V, Paul Mcstay V, George Raptakis V, and Peter Fitzpatrick V. Full Scale Applications of Air Lubrication for Reduction of Ship Frictional Resistance Feasibility of Drag Reduction. 1(V):1–12, 2016.

- [17] Noah Silberschmidt, Dominic Tasker, Takis Pappas, and Johannes Johannesson. Silverstream ® System – Air Lubrication Performance Verification and Design Development. *Shipping in Changing Climates Conference 2016*, pages 1–12, 2016.
- [18] Julio M. Barros Michael P. Schultz Anish Tuteja Marc Perlin Steven L. Ceccio James W. Gose, Kevin B. Golovin. Laser Doppler Velocimetry Measurements of A Turbulent Boundary Layer Flow over Sprayed Superhydrophobic Surfaces. *10th International Symposium on Turbulence and Shear Flow Phenomena (TSFP10), Chicago, USA, July, 2017*, (V):1–12, 2017.
- [19] Sintef ocean. <https://www.sintef.no/en/all-laboratories/towing-tanks/>. Accessed: 14-06-2019.
- [20] Anton paar gmbh. <https://wiki.anton-paar.com/en/water/>. Accessed: 14-06-2019.
- [21] Tommy Ness Torstensen, JOTUN A/S. Personal communication. 2019.

A MPXV7002 Differential Pressure Sensor

MPXV7002 Integrated Silicon Pressure Sensor On-Chip Signal Conditioned, Temperature Compensated and Calibrated

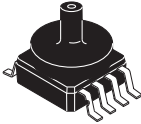
The MPXV7002 series piezoresistive transducers are state-of-the-art monolithic silicon pressure sensors designed for a wide range of applications, but particularly those employing a microcontroller or microprocessor with A/D inputs. This transducer combines advanced micromachining techniques, thin-film metallization, and bipolar processing to provide an accurate, high level analog output signal that is proportional to the applied pressure.

Features

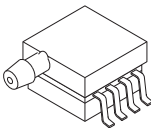
- 2.5% Typical Error over +10°C to +60°C with Auto Zero
- 6.25% Maximum Error over +10°C to +60°C without Auto Zero
- Ideally Suited for Microprocessor or Microcontroller-Based Systems
- Thermoplastic (PPS) Surface Mount Package
- Temperature Compensated over +10° to +60°C
- Patented Silicon Shear Stress Strain Gauge
- Available in Differential and Gauge Configurations

MPXV7002

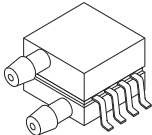
-2 to +2 kPa (-0.3 to +0.3 psi)
0.5 to 4.5 V Output



MPXV7002GC6U/C6T1
CASE 482A

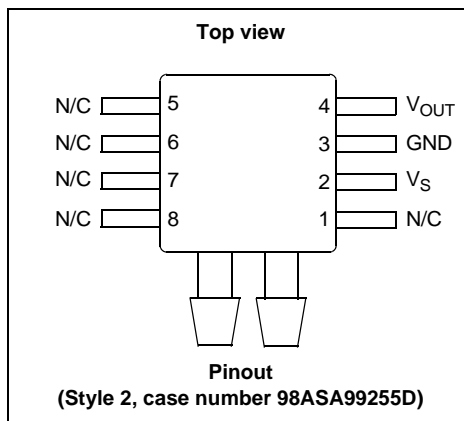


MPXV7002GP
CASE 1369



MPXV7002DP
CASE 1351

Small Outline Package



ORDERING INFORMATION									
Device Name	Package Options	Case No.	# of Ports			Pressure Type			Device Marking
			None	Single	Dual	Gauge	Differential	Absolute	
Small Outline Package (MPXV7002 Series)									
MPXV7002GC6U	Rails	482A		•		•			MPXV7002G
MPXV7002GC6T1	Tape & Reel	482A		•		•			MPXV7002G
MPXV7002GP	Trays	1369		•		•			MPXV7002G
MPXV7002DP	Trays	1351			•		•		MPXV7002DP

1 Operating Characteristics

Table 1. Operating Characteristics ($V_S = 5.0$ Vdc, $T_A = 25^\circ\text{C}$ unless otherwise noted. Decoupling circuit shown in [Figure 3](#) required to meet specification.)

Characteristic	Symbol	Min	Typ	Max	Unit
Pressure Range ⁽¹⁾	P_{OP}	-2.0	—	2.0	kPa
Supply Voltage ⁽²⁾	V_S	4.75	5.0	5.25	Vdc
Supply Current	I_o	—	—	10	mAdc
Pressure Offset ⁽³⁾ @ $V_S = 5.0$ Volts	V_{off}	2.25	2.5	2.75	Vdc
Full Scale Output ⁽⁴⁾ @ $V_S = 5.0$ Volts	V_{FSO}	4.25	4.5	4.75	Vdc
Full Scale Span ⁽⁵⁾ @ $V_S = 5.0$ Volts	V_{FSS}	3.5	4.0	4.5 V	Vdc
Accuracy ⁽⁶⁾	—	—	$\pm 2.5^{(7)}$	± 6.25	% V_{FSS}
Sensitivity	V/P	—	1.0	—	V/kPa
Response Time ⁽⁸⁾	t_R	—	1.0	—	ms
Output Source Current at Full Scale Output	I_{O+}	—	0.1	—	mAdc
Warm-Up Time ⁽⁹⁾	—	—	20	—	ms

1. 1.0 kPa (kiloPascal) equals 0.145 psi.

2. Device is ratiometric within this specified excitation range.

3. Offset (V_{off}) is defined as the output voltage at the minimum rated pressure.

4. Full Scale Output (V_{FSO}) is defined as the output voltage at the maximum or full rated pressure.

5. Full Scale Span (V_{FSS}) is defined as the algebraic difference between the output voltage at full rated pressure and the output voltage at the minimum rated pressure.

6. Accuracy (error budget) consists of the following:

Linearity: Output deviation from a straight line relationship with pressure over the specified pressure range.

Temperature Hysteresis: Output deviation at any temperature within the operating temperature range, after the temperature is cycled to and from the minimum or maximum operating temperature points, with zero differential pressure applied.

Pressure Hysteresis: Output deviation at any pressure within the specified range, when this pressure is cycled to and from the minimum or maximum rated pressure, at 25°C .

TcSpan: Output deviation over the temperature range of 10° to 60°C , relative to 25°C .

TcOffset: Output deviation with minimum rated pressure applied, over the temperature range of 10° to 60°C , relative to 25°C .

Variation from Nominal: The variation from nominal values, for Offset or Full Scale Span, as a percent of V_{FSS} , at 25°C .

7. Auto Zero at Factory Installation: Due to the sensitivity of the MPXV7002 Series, external mechanical stresses and mounting position can affect the zero pressure output reading. Auto zero is defined as storing the zero pressure output reading and subtracting this from the device's output during normal operations. Reference AN1636 for specific information. The specified accuracy assumes a maximum temperature change of $\pm 5^\circ\text{C}$ between auto zero and measurement.

8. Response Time is defined as the time for the incremental change in the output to go from 10% to 90% of its final value when subjected to a specified step change in pressure.

9. Warm-up Time is defined as the time required for the product to meet the specified output voltage after the Pressure has been stabilized.

2 Maximum Ratings

Table 2. Maximum Ratings⁽¹⁾

Rating	Symbol	Value	Unit
Maximum Pressure ($P_1 > P_2$)	P_{max}	75	kPa
Storage Temperature	T_{stg}	-30 to +100	°C
Operating Temperature	T_A	10 to 60	°C

1. Exposure beyond the specified limits may cause permanent damage or degradation to the device.

Figure 1 shows a block diagram of the internal circuitry integrated on a pressure sensor chip.

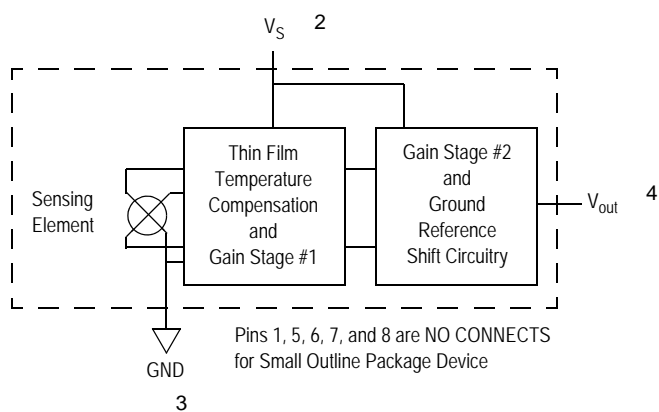


Figure 1. Integrated Pressure Sensor Schematic

3 On-Chip Temperature Compensation, Calibration and Signal Conditioning

The performance over temperature is achieved by integrating the shear-stress strain gauge, temperature compensation, calibration and signal conditioning circuitry onto a single monolithic chip.

Figure 2 illustrates the Differential or Gauge configuration in the basic chip carrier (Case 482). A gel die coat isolates the die surface and wire bonds from the environment, while allowing the pressure signal to be transmitted to the sensor diaphragm.

The MPXV7002 series pressure sensor operating characteristics, and internal reliability and qualification tests are based on use of dry air as the pressure media. Media, other than dry air, may have adverse effects on sensor performance and long-term reliability. Contact the factory for information regarding media compatibility in your application.

Figure 3 shows the recommended decoupling circuit for interfacing the integrated sensor to the A/D input of a microprocessor or microcontroller. Proper decoupling of the power supply is recommended.

Figure 4 shows the sensor output signal relative to pressure input. Typical, minimum, and maximum output curves are shown for operation over a temperature range of 10° to 60°C using the decoupling circuit shown in Figure 3. The output will saturate outside of the specified pressure range.

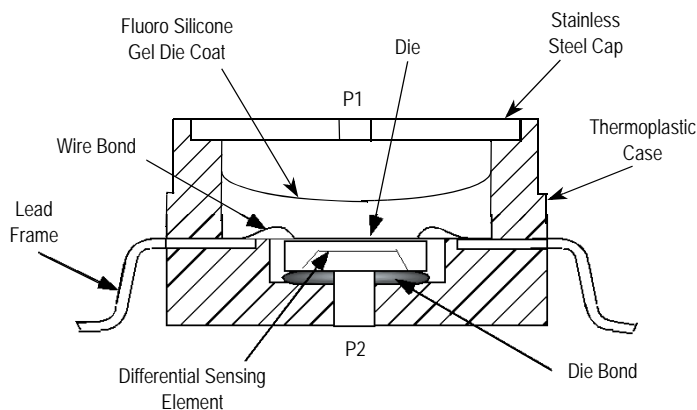


Figure 2. Cross-Sectional Diagram SOP (not to scale)

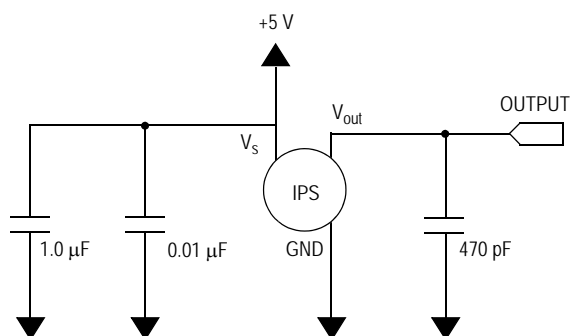


Figure 3. Recommended Power Supply Decoupling and Output Filtering
(For additional output filtering, please refer to Application Note AN1646.)

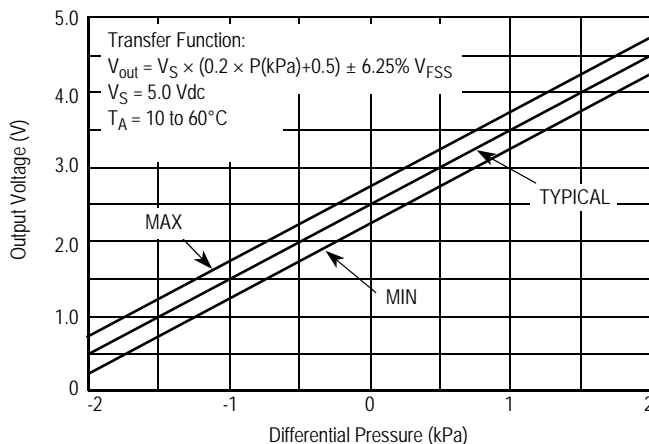


Figure 4. Output versus Pressure Differential

4 Pressure (P1)/Vacuum (P2) Side Identification Table

Freescale designates the two sides of the pressure sensor as the Pressure (P1) side and the Vacuum (P2) side. The Pressure (P1) side is the side containing a gel die coat which protects the die from harsh media.

The Pressure (P1) side may be identified by using the following table:

Part Number	Case Type	Pressure (P1) Side Identifier
MPXV7002GC6U/GC6T1	482A-01	Side with Port Attached
MPXV7002GP	1369-01	Side with Port Attached
MPXV7002DP	1351-01	Side with Part Marking

5 Minimum Recommended Footprint for Surface Mounted Applications

Surface mount board layout is a critical portion of the total design. The footprint for the surface mount packages must be the correct size to ensure proper solder connection interface between the board and the package. With the correct footprint, the packages will self align when subjected to a solder reflow process. It is always recommended to design boards with a solder mask layer to avoid bridging and shorting between solder pads.

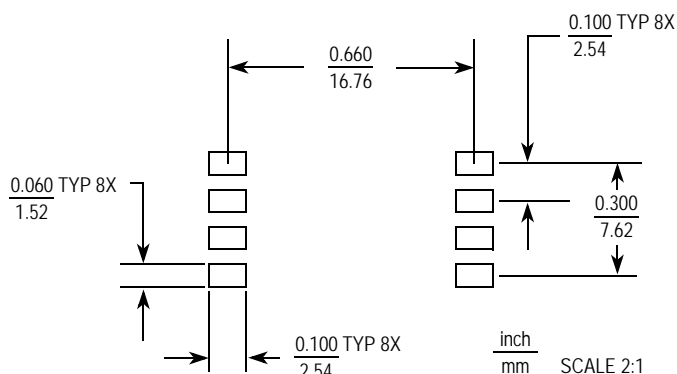
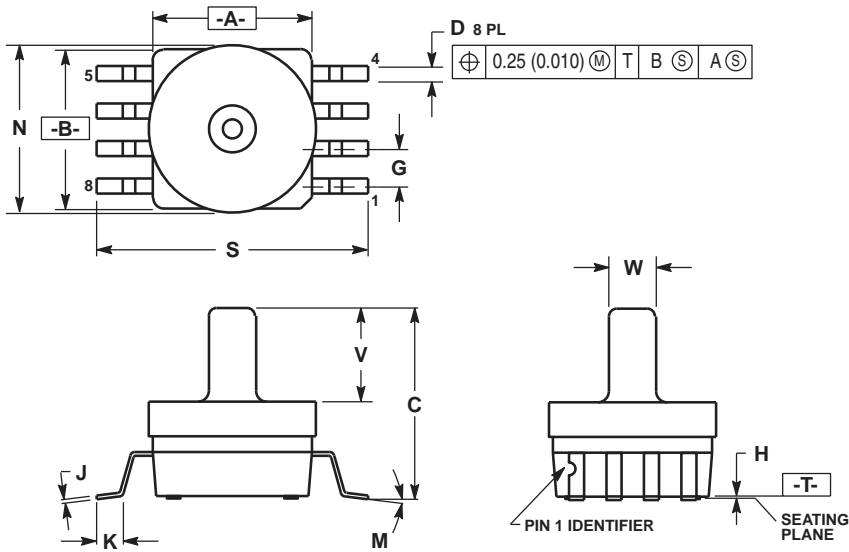


Figure 5. Small Outline Package Footprint

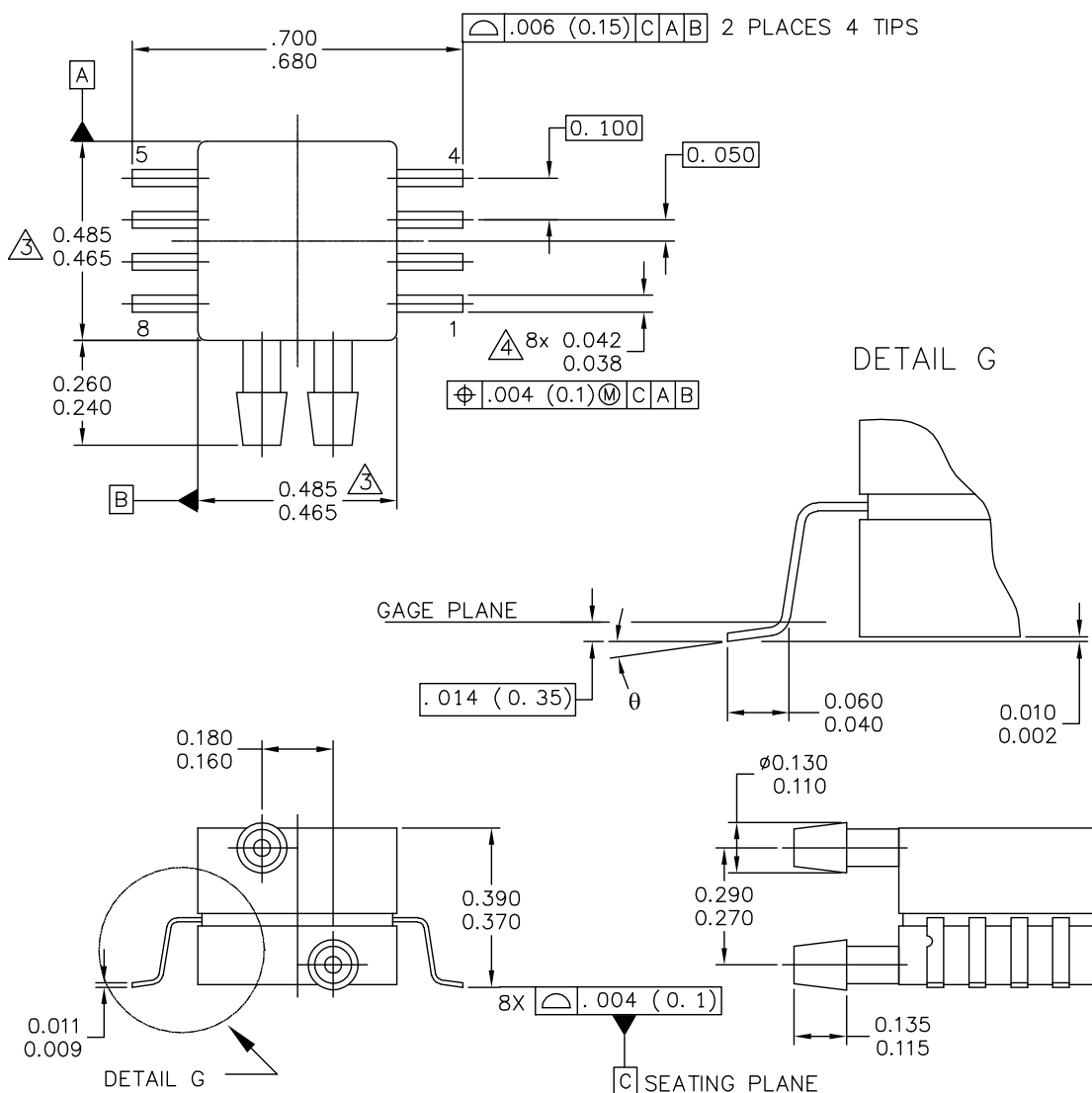
6 Package Dimensions



- NOTES:
1. DIMENSIONING AND TOLERANCING PER ANSI Y14.5M, 1982.
 2. CONTROLLING DIMENSION: INCH.
 3. DIMENSION A AND B DO NOT INCLUDE MOLD PROTRUSION.
 4. MAXIMUM MOLD PROTRUSION 0.15 (0.006).
 5. ALL VERTICAL SURFACES 5° TYPICAL DRAFT.

DIM	INCHES		MILLIMETERS	
	MIN	MAX	MIN	MAX
A	0.415	0.425	10.54	10.79
B	0.415	0.425	10.54	10.79
C	0.500	0.520	12.70	13.21
D	0.038	0.042	0.96	1.07
G	0.100 BSC		2.54 BSC	
H	0.002	0.010	0.05	0.25
J	0.009	0.011	0.23	0.28
K	0.061	0.071	1.55	1.80
M	0"	7"	0"	7"
N	0.444	0.448	11.28	11.38
S	0.709	0.725	18.01	18.41
V	0.245	0.255	6.22	6.48
W	0.115	0.125	2.92	3.17

**CASE 482A-01
 ISSUE A
 SMALL OUTLINE PACKAGE**



© FREESCALE SEMICONDUCTOR, INC. ALL RIGHTS RESERVED.	MECHANICAL OUTLINE	PRINT VERSION NOT TO SCALE	
TITLE: 8 LD SNR, DUAL PORT	DOCUMENT NO: 98ASA99255D	REV: A	
	CASE NUMBER: 1351-01	27 JUL 2005	
	STANDARD: NON-JEDEC		

**CASE 1351-01
ISSUE A
SMALL OUTLINE PACKAGE**

NOTES:

1. CONTROLLING DIMENSION: INCH
2. INTERPRET DIMENSIONS AND TOLERANCES PER ASME Y14.5M-1994.
3. DIMENSIONS DO NOT INCLUDE MOLD FLASH OR PROTRUSIONS. MOLD FLASH AND PROTRUSIONS SHALL NOT EXCEED .006 PER SIDE.
4. DIMENSION DOES NOT INCLUDE DAMBAR PROTRUSION. ALLOWABLE DAMBAR PROTRUSION SHALL BE .008 MAXIMUM.

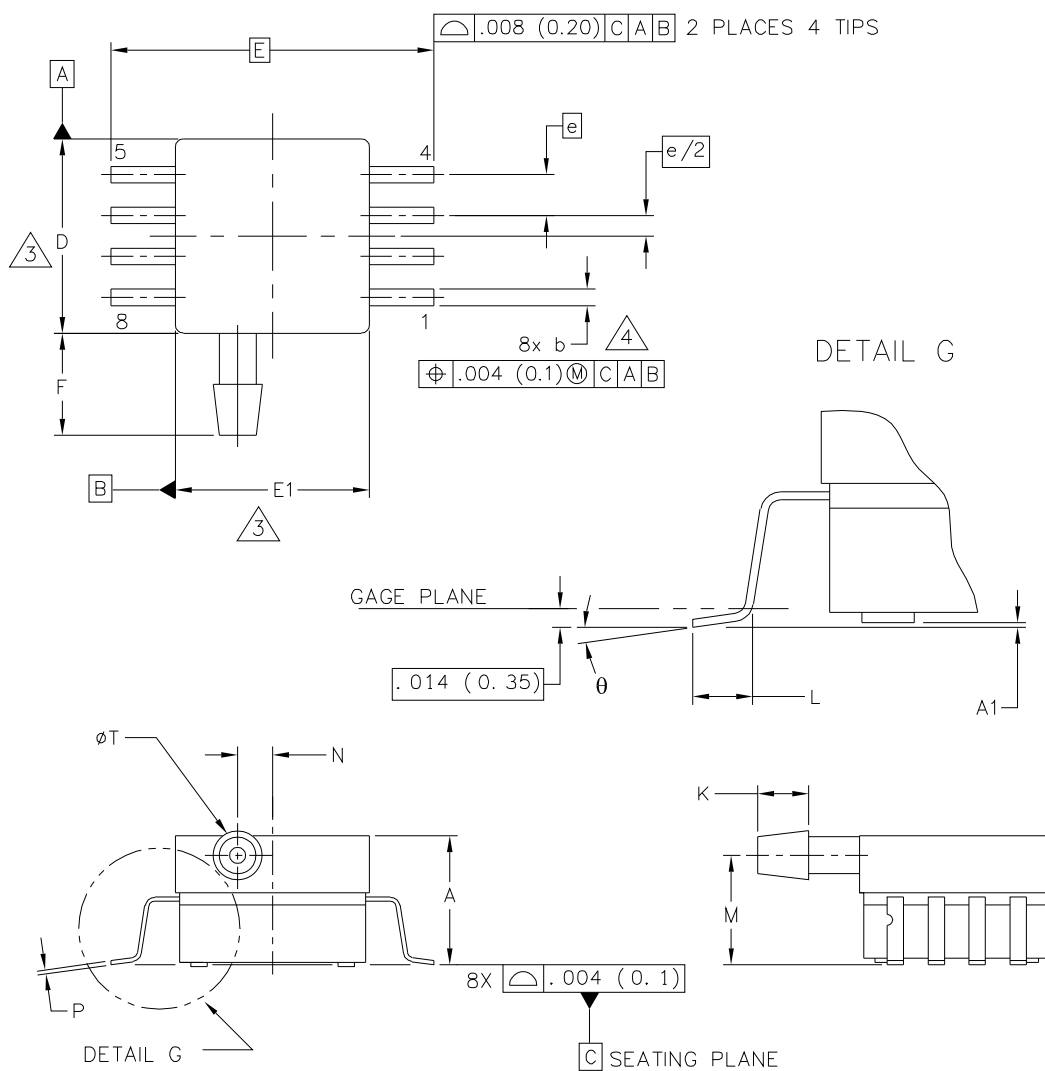
STYLE 1:

PIN 1: GND
 PIN 2: +Vout
 PIN 3: Vs
 PIN 4: -Vout
 PIN 5: N/C
 PIN 6: N/C
 PIN 7: N/C
 PIN 8: N/C

STYLE 2:

PIN 1: N/C
 PIN 2: Vs
 PIN 3: GND
 PIN 4: Vout
 PIN 5: N/C
 PIN 6: N/C
 PIN 7: N/C
 PIN 8: N/C

© FREESCALE SEMICONDUCTOR, INC. ALL RIGHTS RESERVED.	MECHANICAL OUTLINE	PRINT VERSION NOT TO SCALE	
TITLE: 8 LD SNSR, DUAL PORT	DOCUMENT NO: 98ASA99255D	REV: A	
	CASE NUMBER: 1351-01	27 JUL 2005	
	STANDARD: NON-JEDEC		



© FREESCALE SEMICONDUCTOR, INC. ALL RIGHTS RESERVED.	MECHANICAL OUTLINE	PRINT VERSION NOT TO SCALE	
TITLE: 8 LD SOP, SIDE PORT	DOCUMENT NO: 98ASA99303D	REV: D	
	CASE NUMBER: 1369-01	13 DEC 2010	
	STANDARD: NON-JEDEC		


**CASE 1369-01
ISSUE B
SMALL OUTLINE PACKAGE**

NOTES:

1. CONTROLLING DIMENSION: INCH

2. INTERPRET DIMENSIONS AND TOLERANCES PER ASME Y14.5M-1994.

 DIMENSIONS DO NOT INCLUDE MOLD FLASH OR PROTRUSIONS.
MOLD FLASH AND PROTRUSIONS SHALL NOT EXCEED .006 (0.152) PER SIDE.

 DIMENSION DOES NOT INCLUDE DAMBAR PROTRUSION. ALLOWABLE DAMBAR
PROTRUSION SHALL BE .008 (0.203) MAXIMUM.

DIM	INCHES		MILLIMETERS		DIM	INCHES		MILLIMETERS	
	MIN	MAX	MIN	MAX		MIN	MAX	MIN	MAX
A	.300	.330	7.62	8.38	Ø	0'	7'	0'	7'
A1	.002	.010	0.05	0.25	-	----	----	----	----
b	.038	.042	0.96	1.07	-	----	----	----	----
D	.465	.485	11.81	12.32	-	----	----	----	----
E	.717 BSC		18.21 BSC		-	----	----	----	----
E1	.465	.485	11.81	12.32	-	----	----	----	----
e	.100 BSC		2.54 BSC		-	----	----	----	----
F	.245	.255	6.22	6.47	-	----	----	----	----
K	.120	.130	3.05	3.30	-	----	----	----	----
L	.061	.071	1.55	1.80	-	----	----	----	----
M	.270	.290	6.86	7.36	-	----	----	----	----
N	.080	.090	2.03	2.28	-	----	----	----	----
P	.009	.011	0.23	0.28	-	----	----	----	----
T	.115	.125	2.92	3.17	-	----	----	----	----
© FREESCALE SEMICONDUCTOR, INC. ALL RIGHTS RESERVED.			MECHANICAL OUTLINE			PRINT VERSION NOT TO SCALE			
TITLE:					DOCUMENT NO: 98ASA99303D			REV: D	
8 LD SOP, SIDE PORT					CASE NUMBER: 1369-01			13 DEC 2010	
					STANDARD: NON-JEDEC				

**CASE 1369-01
ISSUE B
SMALL OUTLINE PACKAGE**

7 Revision History

Table 1. Revision History

Revision number	Revision date	Description of changes
3	01/2015	<ul style="list-style-type: none"> • Updated data sheet format. • Added Pinout. • Updated package outline for 98ASA99303D.

How to Reach Us:

Home Page:

www.freescale.com

Web Support:

<http://www.freescale.com/support>

Information in this document is provided solely to enable system and software implementers to use Freescale products. There are no express or implied copyright licenses granted hereunder to design or fabricate any integrated circuits based on the information in this document.

Freescale reserves the right to make changes without further notice to any products herein. Freescale makes no warranty, representation, or guarantee regarding the suitability of its products for any particular purpose, nor does Freescale assume any liability arising out of the application or use of any product or circuit, and specifically disclaims any and all liability, including without limitation consequential or incidental damages. "Typical" parameters that may be provided in Freescale data sheets and/or specifications can and do vary in different applications, and actual performance may vary over time. All operating parameters, including "typicals," must be validated for each customer application by customer's technical experts. Freescale does not convey any license under its patent rights nor the rights of others. Freescale sells products pursuant to standard terms and conditions of sale, which can be found at the following address: <http://www.reg.net/v2/webservices/Freescale/Docs/TermsandConditions.htm>.

Freescale and the Freescale logo are trademarks of Freescale Semiconductor, Inc., Reg. U.S. Pat. & Tm. Off. All other product or service names are the property of their respective owners.

© 2015 Freescale Semiconductor, Inc. All rights reserved.

B iRon II Dataset

iRon II- Dataset V.1.0

1. Description of the device

iRon is a NACA0025 shape prototype of a chord length of 220 mm. The prototype has ten differential pressure sensors (1-10, MPXV7002) with a measuring range of ± 2000 Pa and an absolute one (11– MPX5010GP) with a measuring range from 0 to 10000 Pa (10 m of water column) (Figure 1).

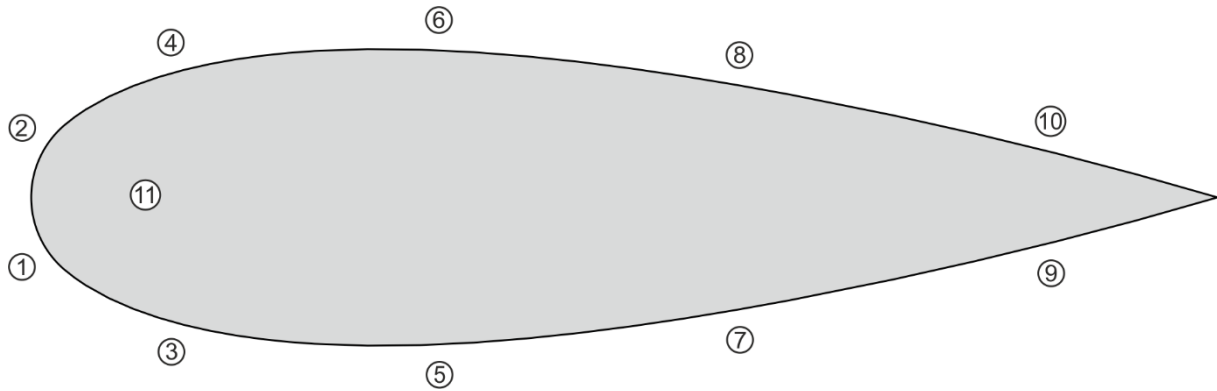


Figure 1. Sensor order and numbering (source: JF Fuentes-Pérez).

The sensors analog output is transmitted into two 8 channels A/D (analog to digital) converter of 16 bits (LTC1867). Due to the target controlled application temperature sensors have not been added to the current prototype. In the future temperature sensors will be added to each of the sensors.

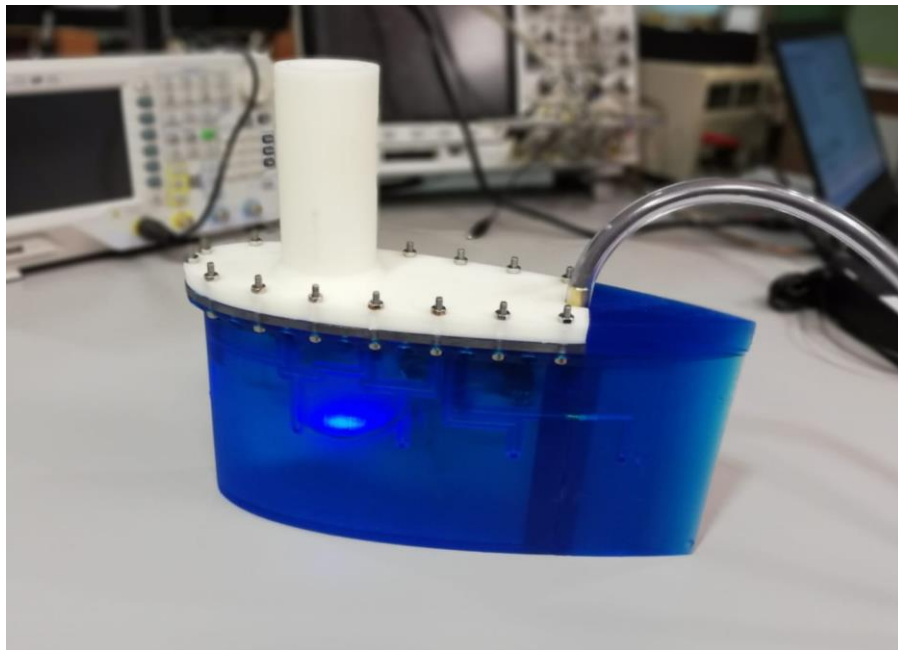


Figure 2. Final prototype after underwater testing (source: JF Fuentes-Pérez).

2. Data

The sampling frequency is programmable; at the moment it is fixed to 200 Hz. Each data line has a time stamp (milliseconds from connection), Ps1, Ps2, Ps3, Ps4, Ps5, Ps6, Ps7, Ps8, Ps9, Ps10 and Ps11 (last correspond to absolute pressure sensor), all of them separated by commas (Figure 3).

```

31 511645,2635,1822,1933,2089,2427,2533,2817,2732,3108,2828,6590
32 511650,2620,1910,1950,2094,2438,2541,2883,2777,3116,2833,6587
33 511655,2734,1989,1912,2120,2442,2542,2846,2803,3121,2835,6596
34 511660,2764,2008,1908,2097,2410,2549,2825,2740,3118,2815,6594
35 511665,2685,1897,1945,2110,2428,2532,2811,2739,3106,2817,6588
36 511670,2571,1812,1926,2080,2412,2536,2848,2747,3106,2827,6591
37 511675,2678,1913,1915,2114,2437,2546,2807,2773,3110,2840,6590
38 511680,2765,2011,1910,2119,2440,2534,2843,2773,3127,2823,6599
39 511685,2734,1962,1933,2096,2422,2566,2828,2726,3100,2816,6593
40 511690,2605,1832,1946,2085,2467,2566,2828,2768,3128,2833,6592
41 511695,2646,1876,1940,2103,2433,2531,2844,2774,3126,2826,6589
42 511700,2733,1983,1912,2077,2398,2554,2869,2758,3121,2831,6595
43 511705,2802,1997,1973,2127,2421,2567,2834,2749,3108,2842,6595
44 511710,2633,1894,1937,2072,2405,2538,2809,2705,3126,2825,6582
45 511715,2602,1831,1930,2099,2422,2561,2838,2774,3114,2825,6587
46 511720,2671,1887,1913,2101,2424,2515,2852,2784,3090,2864,6593
47 511725,2777,2028,1916,2130,2415,2557,2834,2745,3108,2829,6594
48 511730,2696,1946,1944,2100,2465,2536,2875,2758,3116,2829,6595
49 511735,2614,1849,1930,2094,2421,2559,2848,2776,3109,2810,6582
50 511740,2652,1873,1938,2075,2406,2527,2800,2770,3083,2806,6585
51 511745,2697,1918,1946,2092,2441,2553,2788,2760,3079,2865,6585
52 511750,2711,1953,1947,2141,2369,2572,2847,2734,3150,2835,6588
53 511755,2705,1962,1920,2145,2397,2539,2900,2758,3091,2828,6604
54 511760,2653,1888,1907,2080,2452,2528,2840,2728,3103,2803,6583
55 511765,2665,1855,1950,2113,2426,2596,2802,2729,3112,2827,6595
56 511770,2664,1890,1930,2103,2429,2556,2832,2744,3090,2829,6587
57 511775,2711,1953,1921,2131,2415,2550,2850,2744,3104,2820,6595
58 511780,2751,1975,1936,2136,2428,2551,2853,2770,3114,2849,6597
59 511785,2692,1929,1929,2106,2415,2538,2820,2735,3144,2849,6587
60 511790,2665,1923,1945,2118,2431,2530,2826,2730,3150,2842,6590
61 511795,2645,1886,1944,2119,2416,2534,2868,2748,3106,2838,6587
    
```

Figure 3. Data format file from iRon II (source: JF Fuentes-Pérez).

The data from the sensor is raw from the A/D and it has to be translated into Pascal units and, in the same way, a constant offset sensor dependant has to be subtracted. For lab experiments it is recommended to record before each new run¹ a dataset during steady conditions to subtract this constant offset. This file will be used to calculate the offset in each run. Figure 4 shows the dataset processing workflow to be programmed.

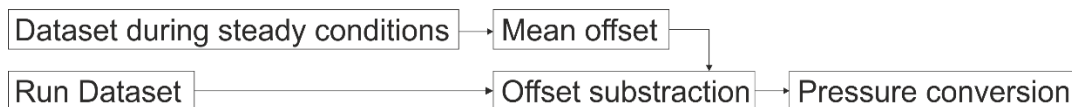


Figure 4. Recommended data processing workflow for the data.

3. Calibration Equations

3.1. Differential pressure sensors

¹ Our experience says that one dataset in steady conditions underwater is enough, however it is highly recommended to record a new one before every new test run.

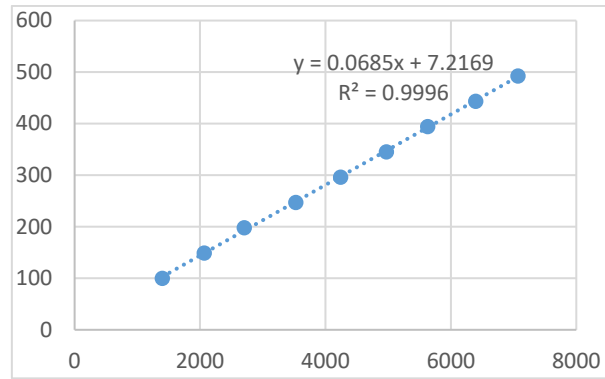


Figure 5. Pascal bit relation for differential pressure sensors

$$\text{Pressure (Pa)} = 0.0685 \cdot (\text{bits} - \text{Offset}) \tag{1}$$

3.2. Absolute pressure sensor

Max A/D converter range = $2^{16} = 65536$ bits (5 v)

Table 1. Test performed in the lab to ensure the correct performance of the electronics

Measured bits	Water column (cm)	Pressure (kPa)	V (according to dataset)	Theoretical bits ¹
2700 (offset)	0	0	0.2 V	2621
6580	62	6.2	0.479 V	6278

¹65536 bits/5 v * 0.2 v = 2621 bits

Assuming linearity (supported but previous test and the dataset):

$$\text{Pressure (Pa)} = 1.6 \cdot (\text{bits} - \text{Offset}) \tag{2}$$

Example: $1.6 \cdot (6580 - 2700) = 6208$ Pa -> 6.2 kPa

C Formlabs Tough Resin Material Data Sheet

MATERIAL DATA SHEET

Tough

Tough Resin for Rugged Prototyping

\$175 / L

Tough Resin balances strength and compliance, making it the ideal choice for prototyping strong, functional parts and assemblies that will undergo brief periods of stress or strain.

Sturdy prototypes

Interference and press fits

Assemblies



FLTOTL05

formlabs 

Prepared 01 . 26 . 2018
Rev 02 01 . 26 . 2018

To the best of our knowledge the information contained herein is accurate. However, Formlabs, Inc. makes no warranty, expressed or implied, regarding the accuracy of these results to be obtained from the use thereof.

Material Properties Data

	METRIC ¹		IMPERIAL ¹		METHOD
	Green ²	Post-Cured ³	Green ²	Post-Cured ³	
Mechanical Properties					
Ultimate Tensile Strength	34.7 MPa	55.7 MPa	5040 psi	8080 psi	ASTM D 638-14
Tensile Modulus	1.7 GPa	2.7 GPa	239 ksi	387 ksi	ASTM D 638-14
Elongation at Break	42 %	24 %	42 %	24 %	ASTM D 638-14
Flexural Strength at 5% Strain	20.8 MPa	60.6 MPa	3020 psi	8790 psi	ASTM D 790-15
Flexural Modulus	0.6 GPa	1.6 GPa	90.3 ksi	241 ksi	ASTM D 790-15
Notched IZOD	32.6 J/m	38 J/m	0.61 ft-lbf/in	0.71 ft-lbf/in	ASTM D256-10
Thermal Properties					
Heat Deflection Temp. @ 1.8 MPa	32.8 °C	45.9 °C	91.1 °F	114.6 °F	ASTM D 648-16
Heat Deflection Temp. @ 0.45 MPa	40.4 °C	48.5 °C	104.7 °F	119.3 °F	ASTM D 648-16
Thermal Expansion (23 – 50 °C)	159.7 µm/m/°C	119.4 µm/m/°C	88.7 µin/in/°F	66.3 µin/in/°F	ASTM E 831-13

¹Material properties can vary with part geometry, print orientation, print settings, and temperature.

²Data was obtained from green parts, printed using Form 2, 100 µm, Tough settings, without additional treatments.

³Data was obtained from parts printed using Form 2, 100 µm, Tough settings and post-cured with 2.5 mW/cm² of 405 nm LED light for 120 minutes at 60°C.

Solvent Compatibility

Percent weight gain over 24 hours for a printed and post-cured 1 x 1 x 1 cm cube immersed in respective solvent:

Solvent	24 hr weight gain (%)	Solvent	24 hr weight gain (%)
Acetic Acid, 5 %	2.8	Hydrogen Peroxide (3 %)	2.1
Acetone	sample cracked	Isooctane	< 1
Isopropyl Alcohol	2.1	Mineral Oil, light	< 1
Bleach, ~5 % NaOCl	1.7	Mineral Oil, heavy	< 1
Butyl Acetate	1.6	Salt Water (3.5 % NaCl)	1.5
Diesel	< 1	Sodium hydroxide (0.025 %, pH = 10)	1.5
Diethyl glycol monomethyl ether	6.6	Water	1.6
Hydraulic Oil	< 1	Xylene	< 1
Skydrol 5	1.2	Strong Acid (HCl Conc)	distorted